Production effects and final-state interactions in $\pi_1 \to 3\pi$

D. Winney,[1,*] S. Gonzàlez-Solís,[2,3] M. Mikhasenko,[4] Ł. Bibrzycki,[5] C. Fernández-Ramírez,[6] V. Mathieu,[2,3] G. Montaña,[2,3] A. Pilloni,[7,8] L. Qiu,[9,10] A. Rodas,[9,10] and A. P. Szczepaniak[9,11,12]

(Joint Physics Analysis Center)

[1]*Instituto de Ciencias Nucleares, Universidad Nacional Autónoma de México, Ciudad de México 04510, Mexico*
[2]*Departament de Física Quàntica i Astrofísica, Universitat de Barcelona, E-08028 Barcelona, Spain*
[3]*Institut de Ciències del Cosmos, Universitat de Barcelona, E-08028 Barcelona, Spain*
[4]*Ruhr University Bochum, D-44801 Bochum, Germany*
[5]*AGH University of Krakow, Faculty of Physics and Applied Computer Science, PL-30-059 Kraków, Poland*
[6]*Departamento de Física Interdisciplinar, Universidad Nacional de Educación a Distancia (UNED), E-28040 Madrid, Spain*
[7]*Dipartimento di Scienze Matematiche e Informatiche, Scienze Fisiche e Scienze della Terra, Università degli Studi di Messina, I-98166 Messina, Italy*
[8]*INFN Sezione di Catania, I-95123 Catania, Italy*
[9]*Theory Center, Thomas Jefferson National Accelerator Facility, Newport News, Virginia 23606, USA*
[10]*Department of Physics, Old Dominion University, Norfolk, Virginia 23529, USA*
[11]*Indiana University, Bloomington, Indiana 47405, USA*
[12]*Center for Exploration of Energy and Matter, Indiana University, Bloomington, Indiana 47403, USA*

(Received 21 July 2026; accepted 26 October 2026; published 18 November 2026)

We investigate the $\pi_1(1600)$ signal channel of 3π in the $J^{PC} = 1^{-+}[\pi\pi]_{1^{--}}\pi P$ wave. This channel has recently been analyzed by the COMPASS collaboration using the "freed-isobar" technique which provides direct experimental access to the line shape modifications of the P-wave $\pi\pi$ subchannel arising from both final state interactions and production processes such as the Deck mechanism. We motivate a unified formalism combining production effects and final state interactions using the Khuri-Treiman formalism, which is consistent with low-energy unitarity, analyticity, and crossing symmetry, seeded by an initial production amplitude. We demonstrate that the precise line shape of the $\pi\pi$ mass spectrum can be used to determine the relative strength and complex phase of different production mechanisms contributing to the 3π final state. We conduct a global fit of the π_1 freed-isobar dataset, yielding a multidimensional parametrization of the $\pi_1 \to 3\pi$ decay amplitude at COMPASS as a function of both decay and production variables. We identify the contributions from short-range production and the Deck mechanism and extract the total 3π invariant mass dependence which will be important for a future extraction of the π_1 pole position in the $\rho\pi$ channel.

DOI: 10.1103/hctz-z2yd

I. INTRODUCTION

The observation of a resonant peak around 1400 MeV in the $\eta\pi$ P-wave mass spectra [1–4] around the turn of the century marked a pivotal point in our understanding of the light hadron spectrum within quantum chromodynamics (QCD). This is because this signal carries exotic quantum numbers $J^{PC}(I^G) = 1^{-+}(1^-)$, which cannot be associated to a $q\bar{q}$ meson. Hence, if the signal corresponds to a resonance, it would thus point unambiguously to an exotic hadron. Similar spin-exotic signals were later observed also in the $\eta'\pi$ [5] and $\rho\pi$ final states [6] at a higher mass of approximately 1600 MeV, pointing to the possibility of two exotic meson states in this sector.

The higher mass state was generally consistent with expectations for hybrid mesons, i.e., states with explicit valence-gluon degrees of freedom in addition to the usual

*Contact author: daniel.winney@nucleares.unam.mx

Published by the American Physical Society under the terms of the Creative Commons Attribution 4.0 International license. Further distribution of this work must maintain attribution to the author(s) and the published article's title, journal citation, and DOI. Funded by SCOAP³.

$q\bar{q}$ structure, which had been postulated as early as the late 1970s [7–10]. More recent lattice QCD studies [11,12] indeed support the existence of a 1^{-+} hybrid meson in the 1.6–2 GeV mass range, coupling predominantly to $b_1\pi$ but also to $\eta^{(\prime)}\pi$ and $\rho\pi$, among others. The presence of two such states, however, was unexpected and pointed to some unknown dynamics complicated by the challenge of isolating exotic signatures and by limited statistics (for a review, see Refs. [13,14]).

In recent years, high-statistics extractions of exotic $\eta^{(\prime)}\pi$ partial waves by the COMPASS Collaboration [15] enabled a simultaneous coupled-channel analysis of both reactions, revealing that the two seemingly distinct peaks arose from a single pole in the complex plane [16]. This supported the existence of a single hybrid, the $\pi_1(1600)$, consistent with lattice predictions. This result was later confirmed by analogous coupled-channel analyses from the Crystal Barrel Collaboration [17,18]. The case of the two apparent π_1 peaks clearly illustrates that investigating multiple decay channels, ideally also multiple production modes, is necessary for a robust understanding of resonance properties.

So far, the only extractions of the π_1 pole position have come from the "golden modes" of $\eta^{(\prime)}\pi$, even though these are predicted to account for only about 2% of the total decay width [12]. The primary reason is that these are two-body final states and thus well suited to rigorous, unitary partial-wave analyses to search for poles on unphysical Riemann sheets. In contrast, the vast majority of the remaining π_1 width is expected to couple to $b_1\pi$ and $f_1\pi$, both of which involve resonances decaying into final states of five or more pions, e.g., in the decay chain $\pi_1 \to b_1\pi \to \omega\pi\pi \to 5\pi$. While the large branching fractions can be exploited to look for exotic signals in previously unobserved production modes, e.g., in photoproduction searches at GlueX [19], a robust pole-search analysis beyond simple bump hunts is functionally impossible in such a multibody final state. This leaves the $\pi_1 \to 3\pi$ decay mode as the largest predicted branching fraction (possibly more than twice that of the combined $\eta^{(\prime)}\pi$), allowing a rigorous exploration of the π_1 properties.

The 3π final state has long been compelling as the simplest three-body hadronic system and thus an ideal laboratory for exploring multibody resonances. Interest has surged more recently due to the possibility of *ab initio* calculations of $3\pi \to 3\pi$ scattering on the lattice, e.g., in Refs. [20–29]. While constructing unitary $3 \to 3$ amplitudes is dramatically more complex than their $2 \to 2$ analogs, recent years have seen significant formal developments in this regard (see, e.g., Refs. [30,31] and references therein).

Unlike on the lattice, three-particle scattering is not directly accessible at experimental facilities, so most data-driven explorations in this sector focus on the production of resonances that then decay into 3π. Of particular note is the COMPASS experiment, which has collected one of the largest 3π datasets to date in its spectroscopy flagship channel of $\pi^- p \to \pi^-\pi^-\pi^+ p$ (an order of magnitude more than in the analogous $\eta^{(\prime)}\pi^-$ production) [32]. Such a large dataset has enabled the development of the novel "freed-isobar" analysis technique, which aims to extract not only 3π partial waves but also the intensity distributions of $\pi\pi$ subchannels projected onto specific quantum numbers in a minimally model-dependent way [33–35]. Applied to the spin-exotic wave in Ref. [36], this technique provides an unprecedented look at 3π dynamics in the $[\pi\pi]_{1^{--}}\pi$ P-wave by capturing possible modifications to the ρ line shape induced by final-state interactions in the mass range of the π_1. Despite its high potential physics impact, the freed-isobar dataset has received relatively little attention because modeling both the high-energy resonance production and the subsequent three-body decay is intricate, making rigorous analysis difficult.

So far, the most successful theoretical formalism for handling 3π decay reactions was proposed by Khuri and Treiman (henceforth KT) [37], in which the three-body decay is assumed to proceed through pairwise interactions. This assumption allows the decay amplitude to be decomposed into crossing-symmetric combinations of isobars, onto which two-body unitarity can be imposed. It has been applied to the decay of a number of (narrow) mesons [38–47]. Despite relying on two-body unitarity relations, the KT construction has been argued to be compatible with three-body unitarity, at least to the extent that the isobar approximation holds [48,49]. The KT formalism can therefore, in principle, be extended to study the three-body mass dependence in systems with more complicated dynamics, such as the π_1 [50–52]. This is especially true when applied to production reactions, where subchannel unitarity is easier to implement than the analogous three-body unitarity [48].

An initial exploration of the $\pi_1 \to 3\pi$ decay using the KT formalism was presented in Ref. [53]. There, the authors focused on the overall importance of the rescattering corrections *per se*. Instead of comparing with existing data, they identified the experimental precision required to distinguish the unitarized line shape (in the form of a once-subtracted solution to KT) from a simpler parametrization that does not incorporate rescattering.

In this work, we take a different approach. Specifically, the presence of a wide π_1 resonance provides sufficient evidence of nontrivial three-body dynamics that should not be ignored. We therefore assume that subchannel line shape modifications arise from rescattering, as a consequence of three-body unitarity implemented by KT. The natural question then becomes: what can be learned about the 3π mass distribution, and therefore about the π_1, from the rescattering effects present in the $\pi\pi$ isobars extracted by COMPASS?

Instead of comparing isobars with and without rescattering effects, we compare the ρ line shapes that arise from the

dynamics of different initial production mechanisms contributing to the final Dalitz plot. This approach allows us to include and identify the key physics at play in the COMPASS data as a function of all relevant kinematic variables, while remaining consistent with low-energy unitarity and analyticity and without arbitrary subtraction polynomials. This work is thus intended as a first step toward extracting the π_1 pole position in the $\rho\pi$ channel.

The rest of the paper is organized as follows: in Sec. II, we describe the decomposition of the $[3\pi]_{1^{-+}}$ Dalitz plot within an isobar model. We also motivate production amplitudes consistent with the isobar picture and relevant for COMPASS kinematics. In Sec. III, we outline how to combine these to implement unitarity using the KT equations, with the production amplitudes as driving terms. The unitarized amplitudes are then compared with data from the freed-isobar analysis in Sec. IV, with a summary and outlook toward future work in Sec. V.

II. ISOBAR DECOMPOSITION AND PRODUCTION AMPLITUDES

At the heart of the KT formalism is the isobar assumption that allows the 3π amplitude to be written as a crossing symmetric combination of analytic functions with only the unitarity cut. As previously mentioned, this formalism is typically applied to narrow resonance decays where the total invariant mass can be considered a fixed value and thus the only relevant dynamics enters only through functions of the subchannel invariant mass. Because of its larger width, a robust exploration of the π_1 requires an amplitude with explicit total 3π mass dependence. One must also account for production effects, such as the Deck mechanism (i.e., $\rho\pi$ production via a pion exchange with a spectator, as in Fig. 1), which will generate logarithmic singularities when projected onto the P-wave and may complicate the identification of the π_1 signal [54–58].

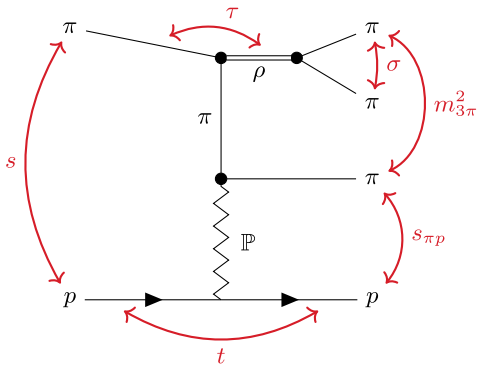


FIG. 1. Diagrammatic representation of the Deck production mechanism at COMPASS and relevant invariant variables. In all plots, π is denoted with single lines, $[2\pi]_{1^{--}}$ by double lines, and $[3\pi]_{1^{-+}}$ by triple lines. The pomeron is denoted by a zigzag and protons by fermion lines.

In this section, we motivate the isobar decomposition for the $[\pi\pi]_{1^{--}}\pi$ P-wave and how to include arbitrary model dependence external to the decay. Such a generalization will allow us to include resonant π_1 line shapes or the Deck mechanism, while staying consistent with low energy analyticity and crossing symmetry and will be the starting point for unitarization via the KT equations in the following section.

Although the full COMPASS process of interest is $2 \to 4$, to ease the connection with the usual KT formalism and the notion of isobars, we begin by motivating the description of the Dalitz plot for the simpler $1 \to 3$ reaction,

$$\pi_1(q) \to \pi(q_a)\pi(q_b)\pi(q_c), \tag{1}$$

where $q^2 = m^2_{3\pi}$, and $q_i^2 = \mu^2$ denotes the mass of the final-state pions.[1] The initial state can be viewed as a shorthand for the projected $[3\pi]_{1^{-+}}$ system at a fixed $m_{3\pi}$ and not necessarily a resonance. We can define the usual invariant-mass variables, which we denote,

$$\sigma_i = (q - q_i)^2 \quad \text{with} \quad i \in \{a, b, c\}, \tag{2}$$

satisfying $\sum_i \sigma_i = 3\mu^2 + m^2_{3\pi} \equiv \Sigma$.

The decay amplitude for the process in Eq. (1) will, in principle, depend on the helicity projection of the π_1 system. However, because the 1^{-+} wave has natural parity, we only need to consider a single scalar amplitude corresponding to a transverse π_1. The decay amplitude can be written in the factorized form [53,59],

$$\begin{aligned}\mathcal{F}(\sigma_a, \sigma_b) &= 2[\epsilon_{\mu\alpha\beta\gamma}\pi_1^\mu q_a^\alpha q_b^\beta q_c^\gamma]\hat{\mathcal{F}}(\sigma_a, \sigma_b) \\ &= \sqrt{\phi}\hat{\mathcal{F}}(\sigma_a, \sigma_b),\end{aligned} \tag{3}$$

where π_1^μ is the polarization vector of the initial state system.[2] We include a factor of two in the normalization to remove overall numerical factors when evaluated in terms of the Kibble function [60],

$$\phi = \sigma_a\sigma_b\sigma_c - \mu^2(m^2_{3\pi} - \mu^2)^2. \tag{4}$$

We note that Eq. (3) has implicit $m_{3\pi}$ dependence, e.g., through the phase space and in Eq. (4). In anticipation of extensions below, we will denote functional dependence on $m_{3\pi}$ (or other kinematic variables) only if it enters through an explicit feature of the model.

The remaining reduced decay amplitude $\hat{\mathcal{F}}$ is related to the scattering process $\pi_1\pi \to \pi\pi$ by crossing symmetry and

[1] We work in the isospin limit with $\mu^2 = m^2_{\pi^+}$ and ignore any complications from isospin breaking effects.

[2] This prefactor is identical to those appearing in $V \to 3\pi$ (see, e.g., [40,43,44]), which also have natural-parity initial states of spin-1.

can thus be decomposed into an expansion in partial-wave amplitudes of definite spin and isospin. In an isobar model, the dominance of two-body subsystems with the lowest spin is used to write a truncated, crossing-symmetric summation (a sketch of this derivation can be found in Appendix A or a fully detailed discussion in Ref. [59]),

$$\mathcal{F}(\sigma_a, \sigma_b) = \sqrt{\phi} \times [F_1^1(\sigma_a) - F_1^1(\sigma_b)]. \tag{5}$$

Here, $F_j^I(\sigma)$ is called an isobar and parameterizes the dynamics of a specific $\pi\pi$ subchannel. For Eq. (5) (i.e., $I = j = 1$), each term describes $\pi\pi$ scattering in P wave with the third pion acting as a spectator. Since this partial wave is dominated by the ρ resonance each isobar can be thought of as the propagation and subsequent decay of the ρ in a two-body subsystem, e.g., in the decay chain $\pi_1 \to \pi[\rho \to \pi\pi]$. The two resonant channels appear with a relative minus sign to ensure the entire amplitude is manifestly crossing symmetric [59].[3]

Isobar functions differ crucially from partial-wave amplitudes in three ways: first, the antisymmetry with respect to $\sigma_a \leftrightarrow \sigma_b$ induces the so-called "isobar ambiguity" where the full amplitude, and therefore the Dalitz intensity, is invariant under the translation by an arbitrary constant (from here on, we drop the indices on the isobars)

$$F(\sigma) \to \alpha + F(\sigma). \tag{6}$$

This invariance reflects an essential ambiguity in isobar decompositions wherein any given isobar (e.g., fixed to data) represents only one of an infinite number of solutions which yield the same total amplitude in Eq. (5). In the present case of the $J^{PC} = 1^{-+}$ quantum numbers, such ambiguity will prevent us from determining the absolute normalization of F from the data.

Second, they are typically assumed to contain only a right-hand cut constrained by (two-body) unitarity and thus to obey m-subtracted dispersion relations of the form,

$$F(\sigma) = P_{m-1}(\sigma) + \frac{\sigma^m}{\pi} \int_{4\mu^2}^{\infty} \frac{d\sigma'}{(\sigma')^m} \frac{\text{Disc}\, F(\sigma')}{\sigma' - \sigma}, \tag{7a}$$

with

$$\text{Disc}\, F(\sigma) = \frac{1}{2i}[F(\sigma + i\epsilon) - F(\sigma - i\epsilon)]. \tag{7b}$$

Due to analyticity, the isobar is determined by its discontinuity, modulo an *a priori* unknown polynomial $P_{m-1}(\sigma)$ that parametrizes effects not fixed by unitarity and must be determined on a process-by-process basis.

Finally, isobars forego the analyticity in angular momentum expected of physical partial-wave amplitudes [61,62]. This means the full amplitude will exhibit unphysical (i.e., non-Regge) behavior when continued to any of the scattering kinematics at high energies. While some of these shortcomings can be overcome with more complex isobar models [63], the simpler dispersive form of Eq. (7) is still expected to be reliable for the decay process in which the π_1 mass limits the physical region of interest well below the model's high-energy breakdown, and in which the unknown subtraction coefficients can be determined by fits to Dalitz plot distributions.

Equations (5) and (7) are the standard starting point for a traditional KT analysis where one absorbs any other effect not determined by unitarity into the unknown subtractions without explicitly modeling them. The isobar assumption itself, i.e., that the process proceeds entirely through pairwise interactions, can be used to include the core features of arbitrary production amplitudes in a straightforward way. Specifically, we consider production and decay to occur in two steps, allowing the replacement [48],

$$F(\sigma) \to F_B(t, m_{3\pi}^2; \sigma) = B(t, m_{3\pi}^2; \sigma) F(\sigma), \tag{8}$$

where, a function B parametrizes the production of quasi-stable $\rho\pi$ and depends on both the running mass of the $[\pi\pi]_{1^{--}}$ subsystem and $m_{3\pi}$ and t are the relevant variables of the production process (e.g., in Fig. 1).[4] The original isobar F then weights the σ distribution with the $\rho \to \pi\pi$ decay line shape. When inserted into Eq. (5), this construction includes production in every possible $\pi\pi$ channel and thus preserves crossing symmetry.

If crossed-channel rescattering can be ignored (e.g., in some systems with large decay mass [53]), then Eqs. (5) and (7) with Eq. (8) are sufficient to construct a 3π production amplitude consistent with low-energy analyticity, unitarity, and crossing symmetry. In this approximation, only the resonant $\pi\pi$ final state scattering is relevant and can be incorporated by imposing "homogeneous" $\pi\pi$ unitarity,

$$\begin{aligned} \text{Disc}_\sigma\, F_B^{(0)}(t, m_{3\pi}^2; \sigma) &= \text{Disc}_\sigma[B(t, m_{3\pi}^2; \sigma) F^{(0)}(\sigma)] \\ &= \sin\delta(\sigma) e^{-i\delta(\sigma)} B(t, m_{3\pi}^2; \sigma) F^{(0)}(\sigma), \end{aligned} \tag{9}$$

[3]For a hypothetical π^0 beam, the $\pi^+\pi^-\pi^0$ Dalitz plot will thus have a ρ^+ and a ρ^- interfering. For the COMPASS π^- beam, two final states are allowed: $\pi^0\pi^0\pi^-$, with two ρ^- interfering, and $\pi^+\pi^-\pi^-$, with two ρ^0 interfering. Regardless, the interference is always destructive.

[4]Being a $2 \to 4$ process it will generally depend on five additional kinematic variables: the total energy of the reaction, s, and solid angles describing the $[3\pi] \to [\pi\pi]\pi$ and $[\pi\pi] \to \pi\pi$ decays. Since we always consider both these systems projected onto definite quantum numbers, this angular dependence is already integrated over. Further as COMPASS measures only a single value of s, we consider it a fixed parameter and do not show functional dependence.

with respect to the P-wave $\pi\pi$ phase shift, $\delta(\sigma)$. We use the superscript to denote the homogeneous solution which will be the Born term, i.e. the "zero-th" iteration, of the full unitarity corrections to be considered in Sec. III.

As, in principle, B represents a 3π production amplitude, it can contain the three-body cut starting at $m_{3\pi}^2 \geq (3\mu)^2$ (e.g., as in Ref. [64]). It, however, does not contain the 2π cut and thus B should contain at most a left-hand cut for $\sigma \leq 0$.[5] This means that above unitarity cut in σ, B will factor from Eq. (9) such that the solution can be written in closed form as the Omnès function [67,68],

$$F_B^{(0)}(t, m_{3\pi}^2; \sigma) = B(t, m_{3\pi}^2; \sigma)\Omega(\sigma), \tag{10a}$$

with

$$F^{(0)}(\sigma) = \Omega(\sigma) = \exp\left(\frac{\sigma}{\pi}\int_{4\mu^2}^{\infty}\frac{d\sigma'}{\sigma'}\frac{\delta(\sigma')}{\sigma'-\sigma}\right). \tag{10b}$$

Here we omit the subtraction polynomial appearing in Eq. (7) which can be absorbed into the production function.

This polynomial is typically used to parameterize ignorance of effects unconstrained by two-body unitarity and in some cases has been matched to fixed-order χPT expansions, as in so-called "reconstruction theorems" (e.g., in Ref. [69]). Insofar as the isobar and elastic rescattering approximations are valid, however, these can only arise from the left-hand cuts induced by production. The typical KT construction therefore assumes these effects are smooth and can be parametrized by a polynomial,

$$B_{m\text{-subs}}(\sigma) = \sum_{i=0}^{m-1} N_i \sigma^i. \tag{11}$$

More physics-motivated (nonpolynomial) functions can be used if the production dynamics is reasonably known (see, e.g., Ref. [70]). In the following, we therefore motivate specific Born terms relevant for the hadroproduction of the π_1 at COMPASS rooted in meson exchange and Regge phenomenology.

A. Short-range production

We first consider the simplest production mechanism for the $[3\pi]_{1^{-+}}$ system, which is direct, local production as in Fig. 2. Unlike Fig. 1, which we will consider below, this mechanism produces the 3π final state coherently and thus mimics the $2 \to 2$ production of a resonance via Pomeron exchange—without microscopic dependence on any of the decay variables. As such, this production process will serve as a baseline with which to identify the general kinematic structure of the reaction and build more complicated production models.

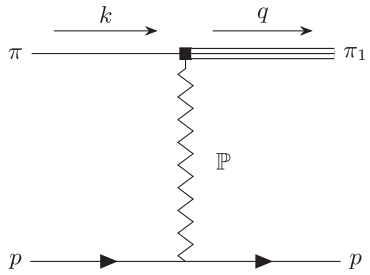


FIG. 2. Diagrammatic representation of contact, resonance-like hadro-production off a proton target.

Because this diagram is mediated by a Regge exchange, it is expected to factorize and thus be readily modeled with effective Lagrangians. The most relevant piece for our purposes is the local $\pi\pi_1\mathbb{P}$ interaction at the "top" vertex for which we write the Lagrangian corresponding to the production of the $M^\epsilon = 1^+$ wave, ignoring numerical factors,

$$\mathcal{L}^{\text{Contact}}_{\pi_1\pi\mathbb{P}} = \epsilon_{\mu\nu\alpha\beta}\pi_1^\mu \partial^\nu \pi \partial^\alpha \mathbb{P}^\beta. \tag{12}$$

As we consider Fig. 2 in the high-energy, near-forward kinematics, we may consider the Pomeron trajectory near $\alpha_{\mathbb{P}}(t=0) \approx 1$ and approximate the Pomeron as a vector field [16,71–74]. As in Eq. (3), the π_1 field acts as a projector for the 3π system of mass $m_{3\pi}$, ensuring that the final-state pions are in the 1^{-+} wave without explicitly integrating over decay angles. Due to parity, we have only this single Lorentz structure.

With this vertex and a generic, helicity-dependent nucleon vector $h^\mu_{\lambda\lambda'}$ parameterizing the "bottom" vertex (its explicit form will not be needed), the amplitude for Fig. 2 can be written as,

$$B_{\text{Contact}}(s, t, m_{3\pi}^2) = N_c(m_{3\pi}^2) s^{\alpha_{\mathbb{P}}(t)} e^{c_0 t}[\epsilon_{\mu\nu\alpha\beta}\pi_1^\mu k^\nu q^\alpha h^\beta_{\lambda\lambda'}], \tag{13}$$

in terms of an arbitrary complex $m_{3\pi}$-dependent normalization,[6] as well as the typical Regge factors associated with the Pomeron trajectory $\alpha_{\mathbb{P}}(t)$ and the expected exponential falloff for diffractive reactions. Note that, because the contact interaction does not depend microscopically on the $\rho\pi$, no arbitrary polynomials of σ can arise, even with more complicated Lagrangians.

The remaining term in the square brackets consists solely of kinematical factors that arise from the helicity structure, e.g., the so-called half-angle factors. In the Regge limit,

[5] In principle, finite cuts in the right-half plane are also possible (see, e.g., Refs. [65,66]) but not relevant for the current discussion as they do not overlap the physical region.

[6] Because the experimental intensity is not absolutely normalized, the mass dimension of N_c will be irrelevant. Still, factors of $s_0 = 1\ \text{GeV}^2$ are assumed wherever appropriate.

relevant for COMPASS kinematics, this entire factor reduces to a power of t that depends on the net helicity at each vertex [61,74]. Specifically, in this limit, we may replace,

$$[\epsilon_{\mu\nu\alpha\beta}\pi_1^\mu k^\nu q^\alpha h^\beta_{\lambda\lambda'}] \longrightarrow \sqrt{-t}^{1+|\lambda-\lambda'|} = \sqrt{-t}, \tag{14}$$

where we assume the dominance of s-channel helicity-conserving interactions between the target and the recoil proton (i.e., $\lambda = \lambda'$). This assumption has been verified in a number of high-energy diffractive production processes involving the Pomeron (e.g., in Refs. [75–77]). Equation (14) indicates that Regge theory requires the t distribution to vanish at forward angles, consistent with the observed event distributions in the initial (not freed-isobar) analysis at COMPASS [78].

Finally, because the freed-isobar data is only available for a fixed value of s, we will not be sensitive to the total invariant mass dependence. We may thus absorb the dependence of the Regge factor into the undetermined parameters by defining $c = c_0 + \alpha'_{\mathbb{P}} \log s$, where we approximate the Pomeron trajectory as linear with slope $\alpha'_{\mathbb{P}}$. This reduces Eq. (13) to

$$B_{\text{Contact}}(t, m^2_{3\pi}) = N_c(m^2_{3\pi})\sqrt{-t}e^{ct}. \tag{15}$$

In principle, if Eq. (15) represents the full production, the pole position of the π_1 can be extracted from knowledge of N_c using explicit three-body unitarity. Additionally, because the short-range production treats the $[3\pi]_{1^{-+}}$ system coherently and contains no σ dependence, it will be functionally equivalent to a constant from the perspective of the KT equations, which are insensitive to overall factors.

B. Deck mechanism

For Deck production, we must consider the microscopic dependence on the $\rho\pi$ system being produced via pion exchange. This can, in principle, be readily calculated by considering the diagram in Fig. 1 and projecting the $\rho\pi$ system onto the P wave, such that,

$$B_{\text{Deck}}(t, m^2_{3\pi}; \sigma) \propto \frac{1}{2}\int_{-1}^{1} dz \frac{1-z^2}{\mu^2 - \tau(z)}, \tag{16}$$

in terms of the momentum transfer $\tau(z)$, which also implicitly depends on $t, m^2_{3\pi}$, and σ [cf. Eq. (B3)]. To draw an analogy to the structure of the contact term of the previous subsection, we will calculate the partial wave using effective Lagrangians, as this will allow a clear identification of the kinematic structure. To this end, we consider the π_1 field as a projector so that Eq. (16) is equivalent to considering the discontinuity of the triangle diagram in Fig. 3, taking σ as the ρ mass squared. As we require that the $\rho\pi$ intermediate state be on shell, the discontinuity of the loop must be taken across the $m_{3\pi}$ cut.[7]

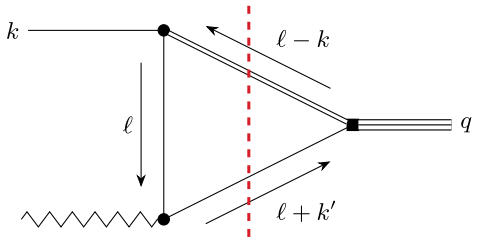


FIG. 3. Feynman loop whose discontinuity corresponds to the Deck projected onto the $1^{-+}\rho\pi$ P-wave. Particle labels are the same as Figs. 1 and 2. $k' = q - k$ and we omit the nucleon vertex which is irrelevant. As we are interested on the amplitude for on-shell $\rho\pi$, we cut the diagram along the red line. The subenergy σ is taken as the ρ mass squared.

Examining Fig. 3, the required vertices are (we again ignore couplings and other numerical factors),

$$\mathcal{L}_{\rho\pi\pi} = i\rho^\mu \pi \overleftrightarrow{\partial}_\mu \pi, \qquad \mathcal{L}_{\mathbb{P}\pi\pi} = i\mathbb{P}^\mu \pi \overleftrightarrow{\partial}_\mu \pi, \tag{17a}$$

and

$$\mathcal{L}_{\pi_1\rho\pi} = \epsilon_{\mu\nu\alpha\beta}\pi_1^\mu \partial^\nu \pi \partial^\alpha \rho^\beta, \tag{17b}$$

noting that the pion-exchange subprocess is of the form $V\pi \to V\pi$. With Eq. (17), one may write the loop in Fig. 3 as

$$\mathcal{T}(t, m^2_{3\pi}; \sigma) = \frac{i}{\pi^2}\int \frac{\mathcal{N}(\ell, q, k) d^4\ell}{[\ell^2 - \mu^2][(\ell - k)^2 - \sigma][(\ell + q - k)^2 - \mu^2]}, \tag{18a}$$

where the numerator is given by,

$$\mathcal{N}(\ell, q, k) = \ell^\mu \ell^\nu [\mathbb{P}_\mu \epsilon_{\nu\alpha\beta\gamma}\pi_1^\alpha k^\beta q^\gamma] \equiv \ell^\mu \ell^\nu \hat{\mathcal{N}}_{\mu\nu}. \tag{18b}$$

We observe that the reduced tensor $\hat{\mathcal{N}}_{\mu\nu}$ depends only on external momenta and obeys the orthogonality relations,

$$(q-k)^\mu \hat{\mathcal{N}}_{\mu\nu} = q^\nu \hat{\mathcal{N}}_{\mu\nu} = k^\nu \hat{\mathcal{N}}_{\mu\nu} = 0. \tag{19}$$

As a result, performing a Passarino-Veltman decomposition [79] of the remaining tensor integral yields only a nonzero contribution proportional to $g^{\mu\nu}$. We can therefore write Eq. (18) as,

$$\mathcal{T}(t, m^2_{3\pi}; \sigma) = [\epsilon_{\mu\nu\alpha\beta}\pi_1^\mu k^\nu q^\alpha \mathbb{P}^\beta] \times \hat{\mathcal{T}}(t, m^2_{3\pi}; \sigma), \tag{20}$$

[7]Cutting the loop diagram will also introduce a P-wave $\rho\pi$ phase space factor, which needs to be removed to not double count the kinematical factors already given by the Kibble function in Eq. (3).

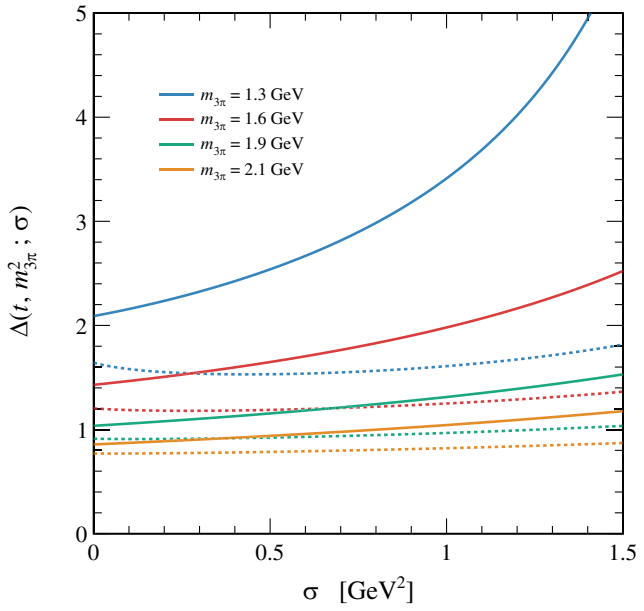


FIG. 4. Dependence of Δ on the various production variables. Solid curves denote fixed $t = t_0 = -0.12$, which is the smallest t-bin considered by the COMPASS analysis, while dashed curves fix $t = t_3 = -0.66$, which is the largest.

where the prefactor is precisely that which arises from Eq. (12) and $\hat{\mathcal{T}}$ is a scalar, logarithmically divergent three-point integral.[8] Cutting this loop, i.e., putting the intermediate state on shell, we have

$$\frac{1}{2i}[\hat{\mathcal{T}}(t, m^2_{3\pi} + i\epsilon; \sigma) - \hat{\mathcal{T}}(t, m^2_{3\pi} - i\epsilon; \sigma)] = \rho_{\pi\rho P}\Delta(t, m^2_{3\pi}; \sigma), \tag{21}$$

where $\rho_{\pi\rho P}$ is the quasi–two body phase space of the $[\pi\pi]_{1^{--}}\pi$ intermediate state in P wave. The remaining function is the P-wave projection of the pion exchange (i.e., on the left-hand side of the cut in Fig. 3),

$$\Delta(t, m^2_{3\pi}; \sigma) = \frac{1}{|\boldsymbol{q}||\boldsymbol{k}|}[(1-\zeta^2)Q_0(\zeta) + \zeta], \tag{22}$$

which is consistent with the ${}^3P_1 \to {}^3P_1$ projection of the one-particle exchange (OPE) as calculated in Ref. [81]. We relegate kinematic definitions and discussion of these expressions to Appendix B but comment that Δ will depend on both t and $m^2_{3\pi}$ as well as σ, as can be seen in Fig. 4.

Matching the structure of Eqs. (20) to (12), with $\hat{\mathcal{T}} \to \Delta$ (i.e., cutting the loop and removing the phase space), the Deck induces an effective "coupling" relative to the contact term, given by,

$$\mathcal{L}^{\text{Deck}}_{\pi_1\pi^{\mathbb{P}}} = \mathcal{L}^{\text{Contact}}_{\pi_1\pi^{\mathbb{P}}} \times \Delta(t, m^2_{3\pi}; \sigma), \tag{23}$$

and thus the driving term can be written in complete analogy to Eq. (15),

$$B_{\text{Deck}}(t, m^2_{3\pi}; \sigma) = N_d(m^2_{3\pi})\sqrt{-t}e^{dt}\Delta(t, m^2_{3\pi}; \sigma), \tag{24}$$

in terms of the function Δ and, in general, different normalization and t slope, N_d and d, respectively.

We briefly comment on three technical aspects implicit in Eq. (24). First, due to the spin factors involved, the loop integral in Eq. (20) is divergent. Taken at face value, a counterterm should be introduced, as in an effective field theory, to remove this divergence and absorb the indeterminacy associated with the UV behavior of the (off-shell) particles propagating inside the loop. The loop, however, is only a tool to more effectively project the pion exchange onto the $1^{-+}[\pi\pi]_{1^{--}}\pi$ P wave. After cutting the loop, the physical, on-shell amplitude of interest has no associated UV divergences or indeterminacies.

Second, similar to Eq. (13), the Regge factor associated with the Pomeron appears as $s^{\alpha_{\mathbb{P}}(t)}$ (and is subsequently absorbed). One might expect the factor to be expressed in terms of the invariant mass of the lower exchange, i.e., $s_{\pi p}$ (cf. Fig. 1). In the present kinematics, however, we are firmly in the single Regge regime, with $s \gg m^2_{3\pi} > |t|$ as the only large mass scale. Thus, we may safely assume $s_{\pi p} \approx s$. This is especially true given that we will be insensitive to details of the recoil proton distribution in the Dalitz plot data.

Finally, in the loop integrand, we assume a simple propagator for the exchanged pion. In similar studies, a phenomenological form factor may be required to parametrize effects arising from the finite size of the exchanged particle, which lead to a steeper momentum-transfer distribution. The COMPASS analysis in Ref. [36], for instance, adds an additional exponential factor to adequately describe the angular distribution within their Deck model. We can mimic this effect by modifying the loop integrand with a customary monopole form factor,

$$\frac{1}{\ell^2 - \mu^2} \longrightarrow \frac{1}{\ell^2 - \mu^2}\left(\frac{\mu^2 - \Lambda^2}{\ell^2 - \Lambda^2}\right). \tag{25}$$

In terms of a cutoff momentum scale $\Lambda > \mu$, which is expected to yield an interaction range $R \approx \Lambda^{-1} = \mathcal{O}(1\text{ fm})$. Inserting this into Eq. (18a), we can use

$$\frac{\mu^2 - \Lambda^2}{(\ell^2 - \mu^2)(\ell^2 - \Lambda^2)} = \frac{1}{\ell^2 - \mu^2} - \frac{1}{\ell^2 - \Lambda^2}, \tag{26}$$

to observe that the effect of a form factor is functionally equivalent to the inclusion of additional production terms involving heavier exchanged particles. Reggeization effects for the exchanges pion similarly can be incorporated as a

[8] In the common notation for one-loop integrals, e.g., used in LoopTools [80], we have $\hat{\mathcal{T}}(t, m^2_{3\pi}; \sigma) = (4/\pi)C_{00}(\mu^2, t, m^2_{3\pi}, \mu^2, \mu^2, \sigma)$.

t-dependent form factor (since s is fixed) and thus can also be included similarly. As discussed in Appendix C, diagrams with heavier exchanges can be effectively absorbed in the contact term and are not included explicitly.

C. Isobar ambiguities in the presence of left-hand cuts

Here we very briefly comment on the issue of the polynomial ambiguity of Eq. (6). In the present formalism, the B terms incorporate additional dynamical features through their dependence on production variables, such as three-body cuts and exchange-particle poles in the crossed channel. This differentiates them from other terms in their analytic structure and gives them an intrinsic physical interpretation. As a result, any redefinition of the form Eq. (6), which must not depend on σ, can only be absorbed by the contact term. This ambiguity would therefore complicate the resolution of the π_1 line shape if only the contact term is considered, because arbitrary $m_{3\pi}$ dependence can be added to $N_c(m_{3\pi}^2)$ while still yielding the same Dalitz plot.

If, on the other hand, we were to expect (or the data suggest) a purely Deck-like production, i.e., one with no need for a contact term, then the ambiguity in Eq. (6) is irrelevant, since no contribution constant in σ will exhibit the left-hand cut and logarithmic singularity of the P-wave projected OPE. When both are considered together, the ambiguity in the contact term is trivially absorbed into the overall normalization of the full amplitude, since only the relative sizes and phases of the terms in Eq. (30) are of physical interest. From this perspective, any process that resolves a microscopic $\rho\pi$ interaction (in this case the Deck mechanism) is, in fact, the key to a meaningful extraction of the $m_{3\pi}$ line shape, since the additional structure resolves the ambiguity of the isobar decomposition.

III. INHOMOGENOUS RESCATTERING CORRECTIONS

With the various forms of the B functions for production mechanisms of interest, we return to the important constraint of unitarity. In a typical KT analysis, the titular "KT equations" arise from requiring that the P-wave projection of Eq. (5) satisfies two-body unitarity [59]. This yields a system of integral equations that encode how the isobars-spectator system must rescatter, as required by both unitarity and crossing symmetry. As argued in early work by Aitchison and Pasquier [48], two-body subchannel unitarity implemented by KT is sufficient to satisfy three-body unitarity. Specifically, the KT formalism provides a model realization of 3π unitarity in which the isobars interact with the spectator pion through iterations of the OPE, without a genuine three-body force (see Ref. [52] and references therein).

Restricting to elastic $\pi\pi$ and allowing isobar-spectator rescattering results in the "inhomogenous" unitarity relation [cf., Eq. (9)]

$$\mathrm{Disc}\, F(\sigma) = \sin\delta(\sigma) e^{-i\delta(\sigma)} [F(\sigma) + \tilde{F}(\sigma)], \tag{27a}$$

with the inhomogeneity

$$\tilde{F}(\sigma) = \int d\sigma'\, K(\sigma,\sigma') F(\sigma'), \tag{27b}$$

given in terms of an angular kernel,[9] K, which depends only on the kinematic structure of the crossing matrix [59]. It is most easily expressed in a kinematic-singularity-free form by multiplying by factors of $\kappa \equiv \kappa(\sigma)$ [cf. Eq. (A4)],

$$\kappa^3 K(\sigma,\sigma') = -\frac{3}{2}[\kappa^2 - (2\sigma' + \sigma - \Sigma)^2]. \tag{27c}$$

In the usual KT treatment, solutions to Eq. (27) can once again be obtained in terms of the Omnès function in Eq. (10b). Specifically, one writes a dispersion relation for the ratio $F(\sigma)/\Omega(\sigma)$ such that the solution to Eq. (27) may be written as

$$F(\sigma) = \Omega(\sigma)\left[\sum_{i=0}^{m-1} N_i \sigma^i + \frac{\sigma^m}{\pi}\int_{4\mu^2}^{\infty} \frac{d\sigma'}{(\sigma')^m} \frac{\sin\delta(\sigma')\tilde{F}(\sigma')}{|\Omega(\sigma')|(\sigma'-\sigma)}\right], \tag{28}$$

where the first term is the homogeneous solution to Eq. (9) with Eq. (11). Equation (28) typically cannot be solved analytically but is particularly amenable to numerical iteration or matrix inversion methods.

Guided by the generalization of the homogeneous case to arbitrary production functions, one might expect that the analogous extension for Eq. (28) simply replaces the polynomial term in Eq. (28) by the function B. Indeed, one can easily see that the modified isobar function F_B introduced in Eq. (8) must satisfy the same unitarity relation as Eq. (27a) at fixed values of production variables and thus admits similar solutions as Eq. (28). Imposing the generalized "boundary condition," that this recovers Eq. (10a) when the inhomogeneity is zero, we arrive at

$$F_B(t, m_{3\pi}^2; \sigma) = F_B^{(0)}(t, m_{3\pi}^2; \sigma) + \Omega(\sigma)\frac{\sigma^m}{\pi}\int_{4\mu^2}^{\infty} \frac{d\sigma'}{(\sigma')^m} \frac{\sin\delta(\sigma')\tilde{F}_B(t, m_{3\pi}^2; \sigma')}{|\Omega(\sigma')|(\sigma'-\sigma)}, \tag{29}$$

where $\tilde{F}_B$ follows from Eq. (27b) except with $F \to F_B$.

As an integral equation, Eq. (29) iterates $\pi\pi$ rescattering in all subchannels to all orders, seeded by the initial production function, as shown diagrammatically in

[9] For a technical discussion of solution strategies, including contour integration over σ' and handling the kinematic singularities that arise, we refer to Appendix D of Ref. [59] or the various Appendixes of Ref. [82].

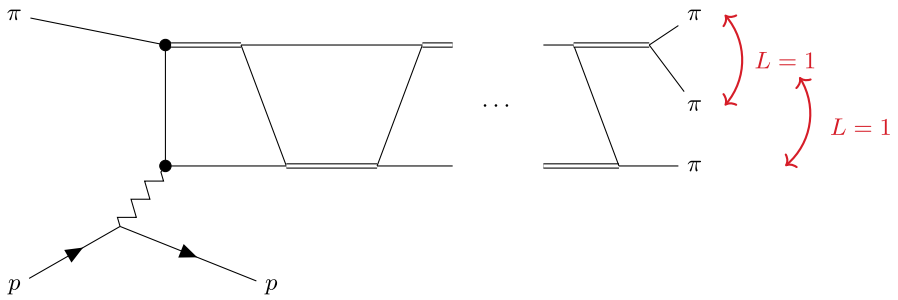


FIG. 5. Diagrammatic representation of the solution to the KT integral equation Eq. (29) with the Deck mechanism as a Born term. The 3π system is at all times projected onto the $1^{-+}[\pi\pi]_{1^{--}}\pi$ P wave such that there is no decay angle dependence [until symmetrized in Eq. (5)].

Fig. 5. The σ dependence introduced by B will therefore determine the specific pattern of modifications which are induced to the ρ line shape by final-state interactions. As a result it is important that the production amplitude can be analytically continued into the complex σ plane for fixed values of the production variables (e.g., as discussed in Appendix B).

Formally, comparing the KT amplitudes with the N/D decomposition in Ref. [83] shows that the left-hand cut contribution introduced by the Born terms is closely related to the numerator amplitude. As a result, from the perspective of 3π unitarity, it is generally not possible to distinguish between resonant and nonresonant production (or, alternatively, signal and background) as is typically done in experimental analyses. A $\rho\pi$ system produced by the Deck process, for instance, can still resonate into the π_1 through final-state interactions.[10]

A. Basis functions

Using the Born amplitudes of Sec. II, we may write a general isobar as Eq. (29), with B given by the sum of Eqs. (15) and (24). We remind that the KT kernel is agnostic to any σ-independent factors, which are functionally constant when solving Eq. (29). This admits a linear decomposition into two basis functions, in which the unknown normalizations and t slopes factor out,

$$F(t, m_{3\pi}^2; \sigma) = N_c(m_{3\pi}^2)\sqrt{-t}e^{ct}F_1(\sigma) + N_d(m_{3\pi}^2)\sqrt{-t}e^{dt}F_\Delta(t, m_{3\pi}^2; \sigma). \quad (30)$$

On the right-hand side, the two basis functions are given by Eq. (29) with $B = 1$ and Δ in Eq. (22), respectively. Equation (30) can be symmetrized as in Eq. (5) to obtain the final amplitude $\hat{\mathcal{F}}(t, m_{3\pi}^2; \sigma_a, \sigma_b)$ and to calculate the four-dimensional intensity. As the basis functions contain no free parameters, they can be precomputed on an arbitrary grid of kinematic variables. Equation (30) is therefore amenable to comparison with data to fix the normalizations and t slopes, as we will see in Sec. IV.

Before then, we first examine these functions in isolation to compare the line shape modifications resulting from each production mechanism. For each Born term and set of production variables, we calculate the basis functions by iterating the KT equations until convergence starting from the homogeneous solution Eq. (10a). As $|\Delta(t, m_{3\pi}^2; \sigma \to \infty)| \propto \sigma^{-1}$, we fix $m = 1$ in Eq. (29) to match the leading asymptotic behavior of the contact term.[11] In all cases, convergence is achieved in ten or fewer iterations.

The simplest isobar is, of course, $F_1(\sigma)$, which is identical to the one that appears in a typical (once-subtracted) KT analysis, e.g., as in Ref. [53]. In this case, the $m_{3\pi}$ dependence appears only through the phase space and thus gives us a glimpse of the minimal three-body mass dependence required by unitarization. The line shape is compared to the unmodified Omnès function in Fig. 6 for various values of $m_{3\pi}$ near the π_1 mass. Here we see that the effects of rescattering corrections are very mild, with deviations in the amplitude squared of a few percent at most.

More interesting is the $m_{3\pi}$ dependence of the isobar driven by Deck production, F_Δ, which we plot in Fig. 7. Here, the additional σ dependence introduced by the Born term, Δ, enhances the rescattering corrections and produces a more pronounced ρ peak that becomes shallower as $m_{3\pi}$ increases. As argued in Sec. II, such a dependence cannot arise from short-range production, even with a more complicated form of the driving term. The Δ function incorporates the effect of the logarithmic singularity of the P-wave-projected pion exchange and thus contributes to all derivatives of the isobar, unlike a typical subtraction polynomial, which determines only the first few terms. Moreover, this "all-orders" contribution to the line shape is not arbitrary, since, for fixed kinematics, the function Δ is fully determined and only the overall normalization is a free parameter.

[10]To illustrate this, we can briefly consider a stable ρ. In the usual N/D formalism, a unitary $\mathbb{P}\pi \to \rho\pi$ amplitude (analogous to the amplitude in Ref. [16]) with two production terms, say $F_{\text{Contact}} + F_{\text{Deck}}$, can be decomposed as $(N_{\text{Contact}} + N_{\text{Deck}})/D_{\rho\pi\to\rho\pi}$, where the π_1 would emerge as a complex root of the (common) denominator.

[11]More detailed discussion of this asymptotic behavior in this limit is relegated to Appendix D.

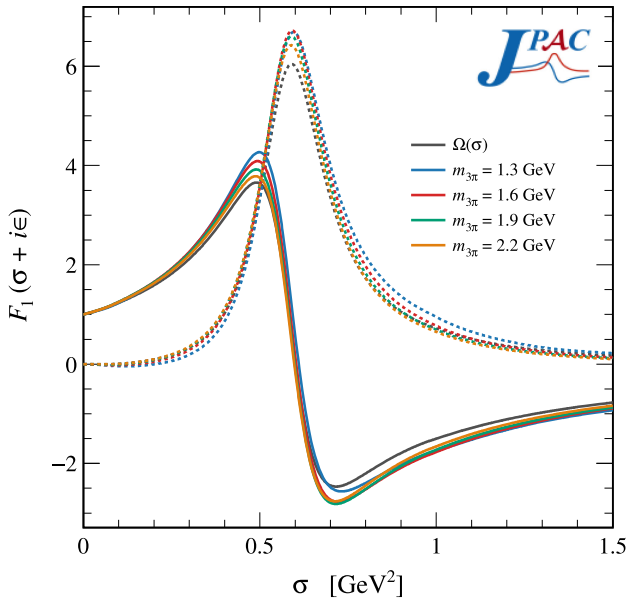


FIG. 6. Real (solid) and imaginary (dashed) parts of the isobar unitarized $F_1(\sigma)$ at various values of $m_{3\pi}$.

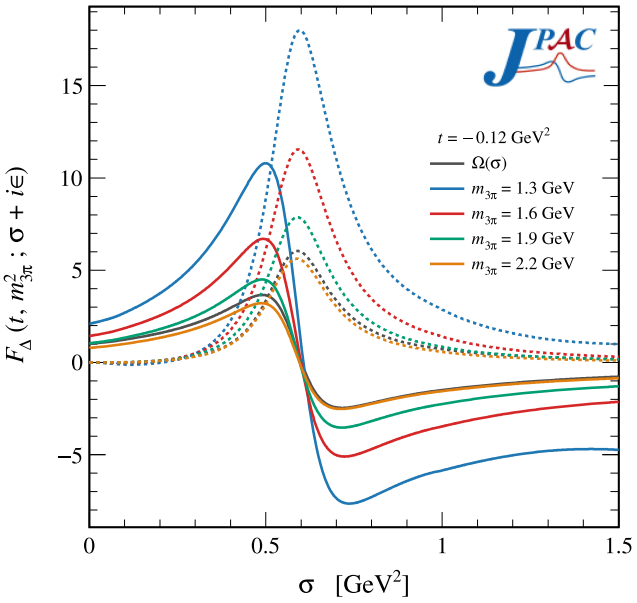


FIG. 7. Analogous to Fig. 6 but for F_Δ. The t-dependence is mild compared to that on $m_{3\pi}$ in the kinematic region of interest and thus we fix $-t = 0.12$ GeV^2.

The size of the modification to the ρ peak resulting from the unitarized Deck diagram compared to that of the contact production suggests that, to the extent that we the isobar approximation holds and we can ignore inelastic effects, the precise line shape in the $[\pi\pi]_{1^{--}}$ mass spectrum at a given $m_{3\pi}$ is diagnostic of the relative strength and phase of the two terms and thus can tell us of the production dynamics as a function of production variables.

IV. ANALYSIS OF FREED-ISOBAR DATA

As argued above, knowledge of the $[\pi\pi]_{1^{--}}$ line shape can be used to constrain the dependence on other production variables. In this section, we do just that by comparing to Dalitz plots generated from the freed-isobar data by COMPASS [36]. Here, an identical decomposition to Eq. (5) is used, except that, instead of assuming a fixed functional form for the isobars, the "freed-isobar" technique assigns each $\pi\pi$ mass bin a floating, complex coefficient using

$$F(\sigma) = \sum_k (F_k^{(\mathrm{Re})} + iF_k^{(\mathrm{Im})})\theta(\Delta\sigma_k - 2|\sigma - \sigma_k|), \quad (31)$$

where σ_k and $\Delta\sigma_k$ denote the center and width of the kth bin. The real and imaginary parts $F_k^{(\mathrm{Re/\,Im})}$ vary with the production variables and are determined by fit [35,36]. The overall complex phase is defined relative to the reference channel, $1^{++}[\pi\pi]_{1^{--}}\pi$ S-wave, but it will not be relevant for this analysis.

By not presupposing a dynamical model, the resulting freed isobars aim to capture all relevant physics information in the event distributions, such as possible rescattering effects, while minimizing model bias. This procedure is repeated for 38 bins in $m_{3\pi}$ spanning [0.98, 2.48] GeV and for 4 bins of $-t$ spanning $[0.1, 0.66]$ GeV^2, yielding the extracted freed isobar as a function of σ on a 2D grid of 152 bins in the production variables.[12]

Because the extracted isobar in Eq. (31) contains information on both modulus and phase, it should, in principle, be directly comparable to the KT isobar in Eq. (30) at the amplitude level. However, because the experimental analysis uses the equivalent of Eq. (5), it is affected by the ambiguity discussed in Sec. II C. A considerable effort is made to resolve this ambiguity in the freed-isobar analysis to visualize the $\pi\pi$-subchannel intensity [34], but ultimately the resulting freed-isobar is just one of infinitely many possible solutions. Because of this, we convert the one-dimensional isobar data back into two-dimensional amplitudes spanning the entire decay region for each value of $(m_{3\pi}^2, t)$,

$$\mathcal{F}^{\mathrm{ex}}(t, m_{3\pi}^2; \sigma_a, \sigma_b) = N_{\mathrm{ex}}\sqrt{\phi} \times \left(\frac{F(\sigma_a)}{Z(\sigma_a)} - \frac{F(\sigma_b)}{Z(\sigma_b)}\right). \quad (32)$$

Here, $Z(\sigma)$ is the so-called zero-mode function, extracted by interpolating the Monte Carlo integral matrix from the experimental analysis [36]. The normalization N_{ex} is chosen such that the experimental integrated intensity,

[12]The data is in bins of $t' = t_{\mathrm{min}} - t$. However, as $s \gg m_{3\pi}^2$ in the COMPASS kinematics, we have $|t_{\mathrm{min}}| \leq 10^{-3}$ GeV^2 and will simply use $-t$ and t' interchangeably.

$$\Gamma^{\rm ex}(t, m^2_{3\pi}) = \sum_{i,j} |\mathcal{F}^{\rm ex}(t, m^2_{3\pi}; \sigma_i, \sigma_j)|^2 \Delta\sigma_i \Delta\sigma_j, \quad (33)$$

matches the total number of events quoted in Ref. [36] for each $(t, m^2_{3\pi})$ bin. The amplitude of Eq. (31) is free of ambiguity as it represents the physical intensity distribution and thus provides a more straightforward comparison with the KT models.

It is important to note that because of the ambiguity, the covariance matrix of the $F_k^{(\rm Re/\,Im)}$'s is nearly degenerate. The nearly degenerate eigenvectors corresponding to the values of $Z(\sigma_k) = Z_k$ are divided out in Eq. (32) to remove the near singularity. For each bin of the four-dimensional intensity, the uncertainty $\delta|\mathcal{F}^{\rm ex}|$ is computed as the standard deviation of 10^3 pseudodatasets resampled within the uncertainties of $F_k^{(\rm Re/\,Im)}$ using the aforementioned correlations [and assuming that $Z(\sigma)$ has negligible uncertainties].

It is important to note that the uncertainties quoted in the COMPASS data are purely statistical and do not account for possible systematic effects which can arise from the freed-isobar analysis. As a result, the data points have generally small and almost certainly underestimated uncertainties. As the systematics of the COMPASS analysis are difficult to estimate, we do not attempt to rescale the original errors but instead consider a re-scaled bootstrapping procedure to attempt a more realistic estimation of own parameter uncertainties (see Appendix F).

A. Single bin fits

Before jumping into a simultaneous fit of 152 Dalitz plots, we begin with exploratory comparisons of single $(m^2_{3\pi}, t)$ bins, which are easier to visualize. To this end, we will fix $t = t_0 \equiv -0.12$ GeV^2, which is the most forward bin in t, and consider a few $m_{3\pi}$ bins around the nominal π_1 mass. At this stage, we treat each bin independently. All t and $m_{3\pi}$ dependence may be absorbed into the normalizations, and thus we may simplify Eq. (30) to,

$$F(\sigma) = N_c F_1(\sigma) + N_d F_\Delta(\sigma), \quad (34)$$

where $N_i = |N_i| e^{i\phi_i}$ are complex. Because we are insensitive to the overall phase, we fit the relative phase $\phi_d - \phi_c$. To compare the features introduced by each term, we will consider three model cases: C, D, and CD which indicate which coefficients are allowed to be nonzero. Model C, for example, sets $N_d = 0$.

For further comparison, we also consider a twice-subtracted solution, as in conventional KT. This corresponds to a solution of the form Eq. (28) with $m = 2$, yielding a decomposition in terms of two basis functions given by Eq. (29) with $B = 1$ and σ, respectively. These basis functions have a different power of m than those in Eq. (34) (because the driving term now goes linearly in σ rather than being asymptotically constant), and thus the two functions with $B = 1$ will differ. We therefore write the conventional KT solution analogous to Eq. (34) as,

$$F(\sigma) = N_0 F'_1(\sigma) + N_1 F'_\sigma(\sigma), \quad (35)$$

where the prime serves only to distinguish these isobars from those appearing in Eqs. (30) and (34). Comparing fit results to Eq. (35) assesses to what extent the effects of additional structure in the driving terms, e.g., the logarithmic singularities of Eq. (24), can be absorbed by subtraction polynomials within the usual KT formalism using the same number of free parameters.

For each model, we minimize

$$\chi^2 = \sum_{k=0}^{n_\sigma - 1} \left(\frac{|\mathcal{F}^{\rm ex}_k| - |\mathcal{F}^{\rm th}_k|}{\delta|\mathcal{F}^{\rm ex}_k|} \right)^2, \quad (36)$$

where k runs over the n_σ bins of (σ_a, σ_b) in the Dalitz plot. The moduli of the amplitudes are computed bin-by-bin from Eq. (3) using Eqs. (32) and (34), for $|\mathcal{F}^{\rm ex}| \pm \delta|\mathcal{F}^{\rm ex}|$ and $|\mathcal{F}^{\rm th}|$, respectively. Results for $m_{3\pi} \in \{1.4, 1.6, 1.8\}$ GeV are tabulated in Tables I and II. We quote only the best-fit value of each parameter since we are only interested in a qualitative assessment of the different models at this stage.

TABLE I. Summary of best-fit values for the different isobar combinations considering independent, single $m_{3\pi}$ bins at fixed $t = t_0 = -0.12$ GeV^2.

	$\lvert N_c\rvert$	$\lvert N_d\rvert$	$\phi_d - \phi_c$	χ^2/d.o.f.
		$m_{3\pi} = 1.4$ GeV		
C	58.1			4.61
D		25.2		4.96
CD	387.5	153.6	−3.00	3.66
		$m_{3\pi} = 1.6$ GeV		
C	29.7			5.80
D		17.2		6.45
CD	326.8	176.6	−3.07	3.47
		$m_{3\pi} = 1.8$ GeV		
C	8.38			3.89
D		6.25		4.07
CD	129.0	92.0	−3.09	3.09

TABLE II. Analogous best-fit values using the conventional twice-subtracted KT parameteization in Eq. (35).

$\lvert N_0\rvert$	$\lvert N_1\rvert$	$\phi_1 - \phi_0$	χ^2/d.o.f.
	$m_{3\pi} = 1.4$ GeV		
1056.8	1760.5	−3.06	3.94
	$m_{3\pi} = 1.6$ GeV		
562.5	929.6	−3.10	4.41
	$m_{3\pi} = 1.8$ GeV		
182.3	325.3	−3.13	3.36

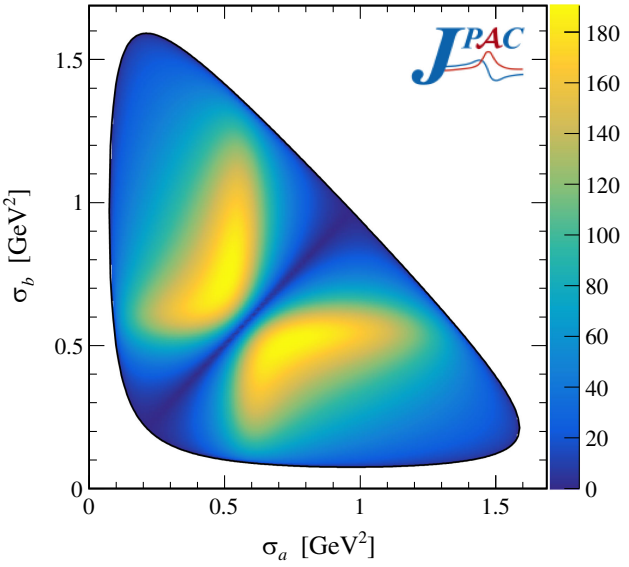


FIG. 8. Dalitz plot intensity using the CD isobar at $m_{3\pi} = 1.4$ GeV and $t = t_0 = -0.12$ GeV^2.

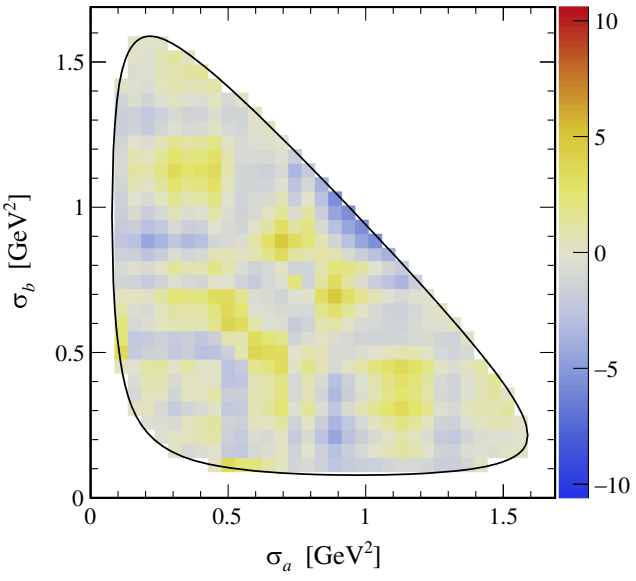
In these comparisons, several points become apparent: first, the CD model, plotted in Fig. 8, substantially improves upon both the contact-only and Deck-only models across all cases. This confirms that Deck production contributes non-negligibly to the COMPASS intensity. We also note that the relative phase between the contact and Deck terms is nearly $-\pi$, so the two terms interfere almost entirely destructively.

Compared with the twice-subtracted KT solution, the CD model fits 10%–30% better in all cases with the same number of free parameters. The largest deviation occurs at the nominal π_1 mass, supporting the more physics-motivated form of the Deck driving term as capturing more essential dynamics in the data. Regardless, both CD and conventional KT have rather large χ^2 per degree of freedom, $\chi^2/\text{d.o.f.} \approx 3-4$. Even a thrice-subtracted KT solution does not appreciably improve the description beyond 15% over Eq. (35). Examining the pull distributions, e.g., of the CD model in Fig. 9, shows no noticeable regions of systematic disagreement between the model and the data. Instead, the residuals show a uniformly large spread, centered at zero, across the entire physical Dalitz region.

These observations point to an adequate description of the current dataset—at least to the degree that the unknown systematic uncertainties of the freed-isobar analysis can be ignored. More specifically, these results highlight the CD model as capturing the essential features present in the data distributions. We also remind that the normalizations of Eq. (34) have a straightforward physical interpretation, i.e., as the product of couplings and line shapes associated with each production term, unlike the coefficients appearing in Eq. (35). This will allow us to learn substantially more, such as the t and $m_{3\pi}$ distributions, when fitting multiple bins simultaneously.

B. Global fit

We now turn to a more detailed analysis of the COMPASS dataset in its entirety. The linearity of the basis functions in Eq. (30) allows us to precalculate them across the entire grid of production variables spanning the



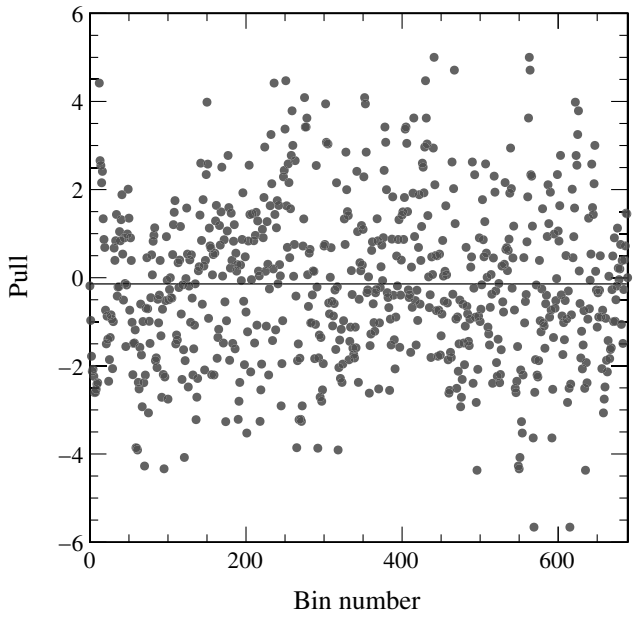


FIG. 9. 2D (left) and 1D (right) pull distributions corresponding to the $t = t_0$, $m_{3\pi} = 1.4$ GeV bin with the CD isobar. We see the large $\chi^2/\text{d.o.f.} = 3.66$ is not driven by a systematic deficiency of the model biasing the curves. In the 1D distribution, the horizontal axis refers to the index when scanning bins in the Dalitz plot from left to right and bottom to top and the horizontal line denotes the average pull.

available data. The normalizations, which are expected to be functions of the $[3\pi]_{1^{-+}}$ mass, can then be extracted by associating a floating complex coefficient to each bin, to be determined by fit—similar to the methodology of the freed-isobar analysis itself. This will allow us to determine the $m_{3\pi}$ dependence directly from the data, without bias from an explicit dynamical model. We therefore fit Eq. (30) in a binned form,

$$F(t, m_{3\pi}^2; \sigma) = \sum_{k=0}^{n_{3\pi}-1} \theta(\Delta m_{3\pi}^2 - 2|m_{3\pi}^2 - m_{3\pi,k}^2|) \times \sqrt{-t}[N_{c,k} e^{c(t-t_0)} F_1(\sigma) + N_{d,k} e^{d(t-t_0)} F_\Delta(t, m_{3\pi,k}^2; \sigma)], \quad (37)$$

where the sum runs over each bin centered at $m_{3\pi,k}^2$ with width $\Delta m_{3\pi}^2$ [cf. Eq. (31)].

Although the t distribution of the data is also binned, the dependence on t enters primarily through the exponential functions, which, for simplicity, we assume share universal, constant slope parameters. We therefore do not need to discretize c and d but do subtract t_0 in the exponent so that this factor is unity at the most-forward bin. Because each $m_{3\pi}$ bin is almost independent, connected only by the t slopes, every $N_{c,d}$ will be highly correlated with c and d but only weakly correlated with each other. By normalizing the exponent this way, we help decouple this factor from the other parameters, leading to better fit convergence.

All in all, considering $n_{3\pi}$ bins of $m_{3\pi}$ requires $3n_{3\pi} + 2$ real parameters, which we fix via a simultaneous fit of the bins. Because the datasets have different numbers of subchannel bins as a function of $m_{3\pi}$, we minimize the average χ^2/n_σ per Dalitz plot,

$$\bar{\chi}^2 = \frac{1}{4n_{3\pi}} \sum_{k=0}^{4n_{3\pi}} \left[\frac{\chi^2}{n_\sigma}\right]_k, \quad (38)$$

where we also include each of the available t bins for every $m_{3\pi}$ value. Each χ^2 is calculated using Eq. (36) and then divided by the number of subchannel mass bins. This prevents the fit from being biased toward the higher $m_{3\pi}$ region, which has larger phase spaces and thus more bins per Dalitz plot.

We fit all $n_{3\pi}$ bins available except for the two bins with smallest total mass, i.e., $m_{3\pi} = 0.96$ and 1 GeV. Initial studies of the ρ peak observed that the nominal ρ mass appears shifted by upwards of 30 MeV in these small $m_{3\pi}$ bins [84] and thus difficult to fit with a model with a fixed ρ position given by the $\pi\pi$ phase shift. This shift results in much larger local best-fit χ^2 indicating these two bins are particularly incompatible with the remaining data (fits to these $m_{3\pi}$ bins alone have $\chi^2/\text{d.o.f.} > 15$) and are thus discarded.

The resulting bin-by-bin normalization values are plotted in Fig. 10, where we see a remarkably (albeit not perfectly) smooth $m_{3\pi}$ dependence. This smoothness is a direct result of considering all t bins simultaneously, as the universal slopes connect and set a scale for the otherwise completely independent bin-wise normalizations. Because the data suggest strong destructive interference, individual t bins constrain only the difference between the two terms, while N_c and N_d can both be arbitrarily large. Fits without the exponential factor therefore yield scatter plots that are sporadic and featureless across the $m_{3\pi}$ range, because

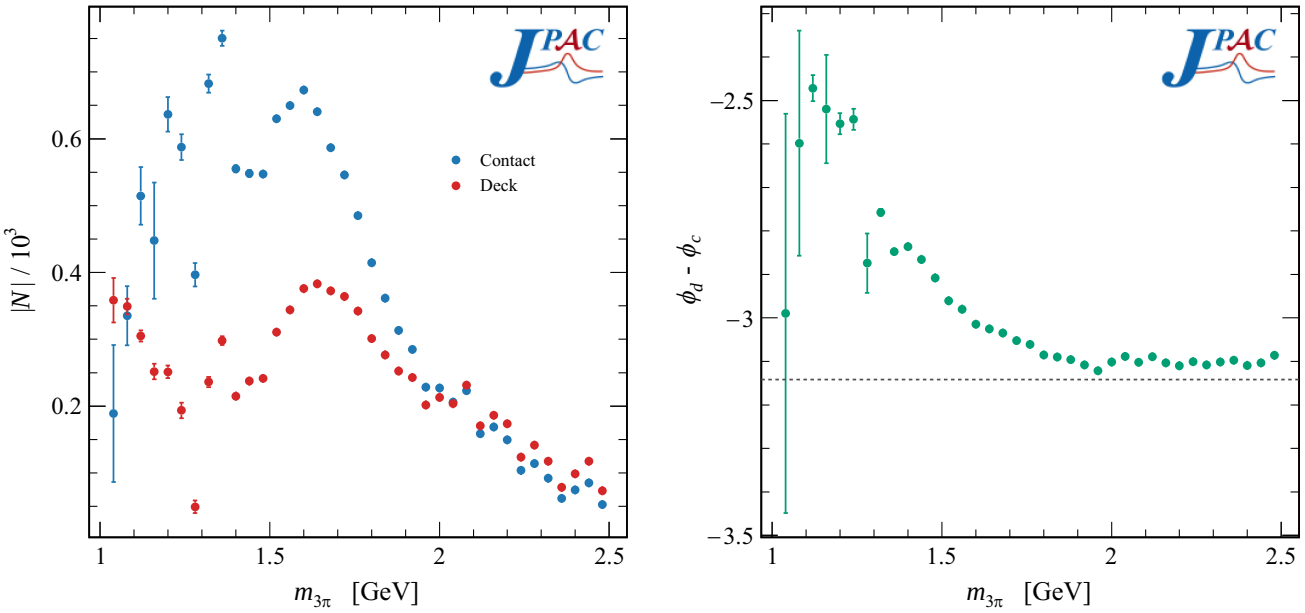


FIG. 10. Extracted distributions of the moduli, $|N_c|$ and $|N_d|$ (left) and relative phase $\phi_d - \phi_c$ (right), as a function of $m_{3\pi}$ resulting from the global fit to COMPASS isobar data. All points include bootstrapped error bars even if they appear too small to see.

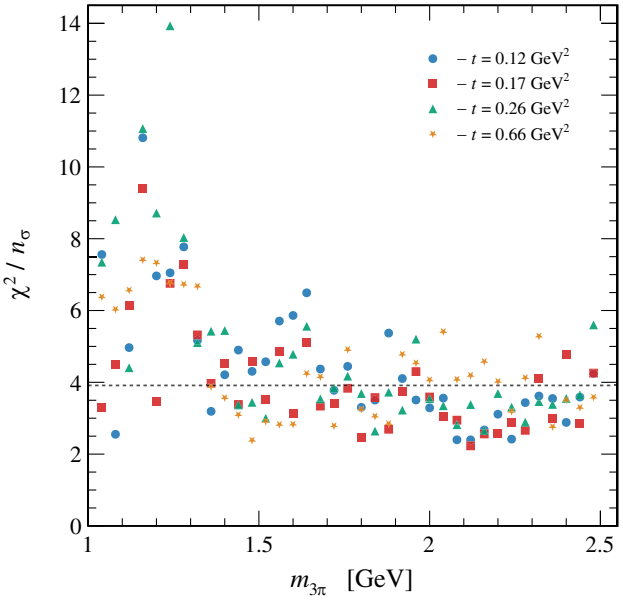


FIG. 11. Distribution of χ^2/n_σ for every Dalitz plot bin considered in the global fit. The dashed line denotes the best-fit $\chi^2/\text{d.o.f.} = 3.91$.

adjacent bins are entirely uncorrelated. The largest deviations from a smooth curve occur toward the ends of distribution and particularly at the low $m_{3\pi}$ range.

The spread of χ^2/n_σ for each of the 144 Dalitz plots is also shown in Fig. 11. Here, we see a substantial spread of χ^2 values, yielding $\bar{\chi}^2 = 4.41$. We note that the region of $m_{3\pi} \leq 1.4$ GeV appears to be slightly less well described than the rest of the bins. This becomes more apparent when calculating the best-fit $\chi^2/\text{d.o.f.} = 3.91$, which weights the low-$m_{3\pi}$ bins (with smaller n_σ's) less heavily, resulting in $\chi^2/\text{d.o.f.} < \bar{\chi}^2$ by 10%.[13]

The quality of the description in the small $m_{3\pi}$ region is likely affected by two effects present in the COMPASS data. First, the measured integrated intensity as a function of $m_{3\pi}$ shows prominent fluctuations among bins below the nominal π_1 mass (cf. Fig. 8 of Ref. [36]). As we should anticipate a mostly smooth distribution, the large deviations, several standard deviations between adjacent $m_{3\pi}$ bins, point to prominent systematic uncertainties in this region which have not been estimated. Second, Ref. [33] previously noted that this $m_{3\pi}$ range has a different characteristic t distribution, preventing a good description in terms of the sum of two exponentials with constant t slopes. This may indicate contributions from other production diagrams not considered, which introduce additional t dependence beyond that in our minimal model.

[13]Fitting only bins with $m_{3\pi} > 1.4$ GeV, for instance, yields $\bar{\chi}^2 = 3.70$ and $\chi^2/\text{d.o.f.} = 3.64$ with nearly identical parameter distributions to those in Fig. 10. This indicates that the larger $\bar{\chi}^2$ of the full fit does not significantly affect the shape of the higher-energy tail.

In order to gauge the effect of additional t dependence, we explore fits with an additional contact term beyond the minimal model in Appendix E. The presence of a third t slope improves the overall fit quality slightly but the χ^2/n_σ distribution still reveal a systematically worse description of the small $m_{3\pi}$ region, pointing to some other systematic effect present in these bins.

The uncertainties of each parameter are estimated using a bootstrap analysis [85]. Because the quoted experimental uncertainties are so small (and the corresponding residuals so large), we generate bootstrap pseudo-datasets by resampling within the local distance to the best-fit model curve (instead of the raw experimental error). This procedure is described in more detail in Appendix F and is expected to yield a more conservative, and therefore *slightly* more realistic, estimate of uncertainties. Despite this rescaling, the resulting bootstrap errors remain unrealistically small and will require further consideration, which we defer to a subsequent analysis.

Examining the distributions of the normalizations themselves, the most glaring feature are the apparent peaks in both normalizations, which are highly suggestive of the resonant π_1. While it may be tempting to fit these distributions with Breit-Wigner amplitudes, a rigorous identification with the π_1 pole requires model parametrizations of $N_c(m^2_{3\pi})$ that can be analytically continued to unphysical Riemann sheets below the three-body cut. The parametric distributions observed in Fig. 10 may thus serve to constrain such a model to extract the π_1 pole parameters. As construction and analytic continuation of three-body amplitudes can be quite delicate (see, e.g., Ref. [66]), this is left for a dedicated follow-up work.

We note the nontrivial dependence on $m_{3\pi}$ that emerges in the Deck coefficient, including an apparent zero around 1.3 GeV. The error bars of these parameters are also generally smaller error bars than those of the contact term, even in the small total mass region. As discussed in Sec. III A, the Deck coefficient is nearly entirely determined by the existence of deformations of the ρ away from the line shape observed in $\pi\pi$ scattering. and thus the distribution in $|N_d|$ emerges from the nontrivial $m_{3\pi}$ dependence of the rescattering corrections captured by the freed-isobar analysis.

Examining the phase difference in Fig. 10, we observe a very smooth and relatively slow-varying phase motion, even around the nominal π_1 mass. If the peaks observed in the normalizations are indeed caused by the π_1, then it must couple to both production mechanisms in order for the characteristic resonant phase motion to cancel in the difference.

The phase difference stays near $-\pi$ for most of the energy range with a monotonic increase at the low $m_{3\pi}$ end, suggesting a characteristically different interference pattern between the two terms for $m_{3\pi} \leq 1.4$ GeV. Plotting the theoretical integrated intensity,

$$\Gamma(t, m_{3\pi}^2) = \int d\sigma \int d\sigma' |\mathcal{F}(t, m_{3\pi}^2; \sigma, \sigma')|^2, \quad (39)$$

as a function of t in Fig. 12 reveals that this phase motion coincides with the region where the contact term is up to an order of magnitude smaller than the Deck contribution. As t increases, the intensity distribution is flatter with the two production terms of similar size with strong destructive interference, as previously observed in Sec. IV A.

The best-fit t slopes are given by,

$$c = 2.860 \pm 0.004 \text{ GeV}^{-2}, \quad (40a)$$

$$d = 2.741 \pm 0.005 \text{ GeV}^{-2}, \quad (40b)$$

which, as they are the only parameters constrained by global features of the data, have very small deviations when bootstrapped. We remind that c and d include the absorbed Regge factor of the $\mathbb{P}$ that may be subtracted to extract the purely exponential t-slope of Eq. (13). Using $\alpha'_{\mathbb{P}} = 0.25 \text{ GeV}^{-2}$ [86] and $s = (19 \text{ GeV})^2$ [36], we obtain central values of

$$c_0 = 1.39 \text{ GeV}^{-2} \quad \text{and} \quad d_0 = 1.27 \text{ GeV}^{-2}. \quad (41)$$

These are generally within expectations for the diffractive peaks in other Pomeron-driven reactions, such as high-energy heavy vector meson photoproduction [87]. It is important to note that although $d \lesssim c$, the Deck contribution can still be seen (e.g., in Fig. 12) to fall off faster than the contact due to the extra t dependence built into Δ in Eq. (22). Even so, the falloff of the Deck term is still comparable to the contact term and thus unlike the t dependence of the nonresonant background models in COMPASS analyses [36,78].

The interplay between the two terms can be illustrated when examining the integrated intensity as a function of $m_{3\pi}$ in each of the t bins in which data is available, which we plot in Fig. 13. Here we see the contributions from the two terms are very similar peaks with the combined intensity driven primarily by large destructive interference. In the most forward-t bin the distributions are nearly identical as needed to produce the peak-less distribution of the data. As t increases, the difference between Deck and contact curves grows revealing the resonancelike peak in the data with largest t.

We reiterate that although the integrated intensities show large destructive interference, this is not the result of a fine-tuned difference between the two production terms. This interference instead emerges from fitting the four-dimensional Dalitz plot data with the Deck constrained by the subtle modifications of the ρ line shape. Indeed, the apparent smoothness of the resulting parameter and intensity distributions across $m_{3\pi}$ bins, despite no by-hand constraint of continuity in the fitting procedure (beyond universal t slopes), as well as Gaussian-like bootstrap distributions without nearby local minima point to this being a robust feature of our model.

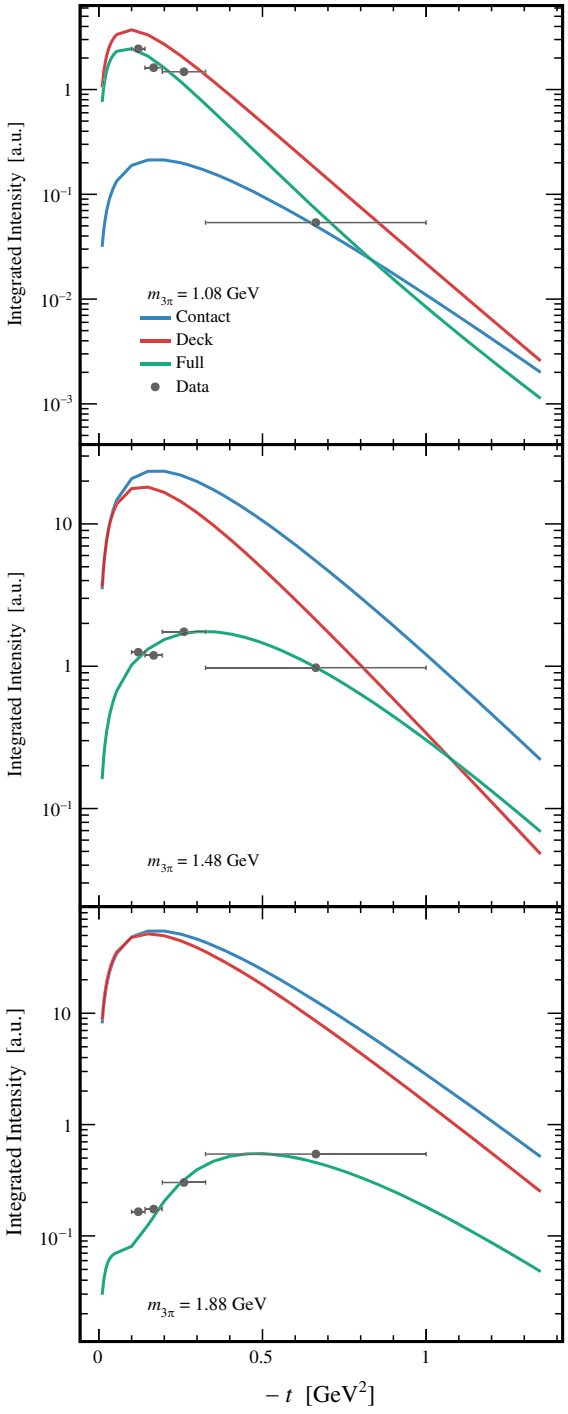


FIG. 12. Integrated width as a function of $-t$ at various characteristic values of $m_{3\pi}$ for the minimal fit results. In addition to the best-fit results (blue) we plot the contributions to the width from individual components. Bootstrapped uncertainties are very small and thus we do not plot error bands.

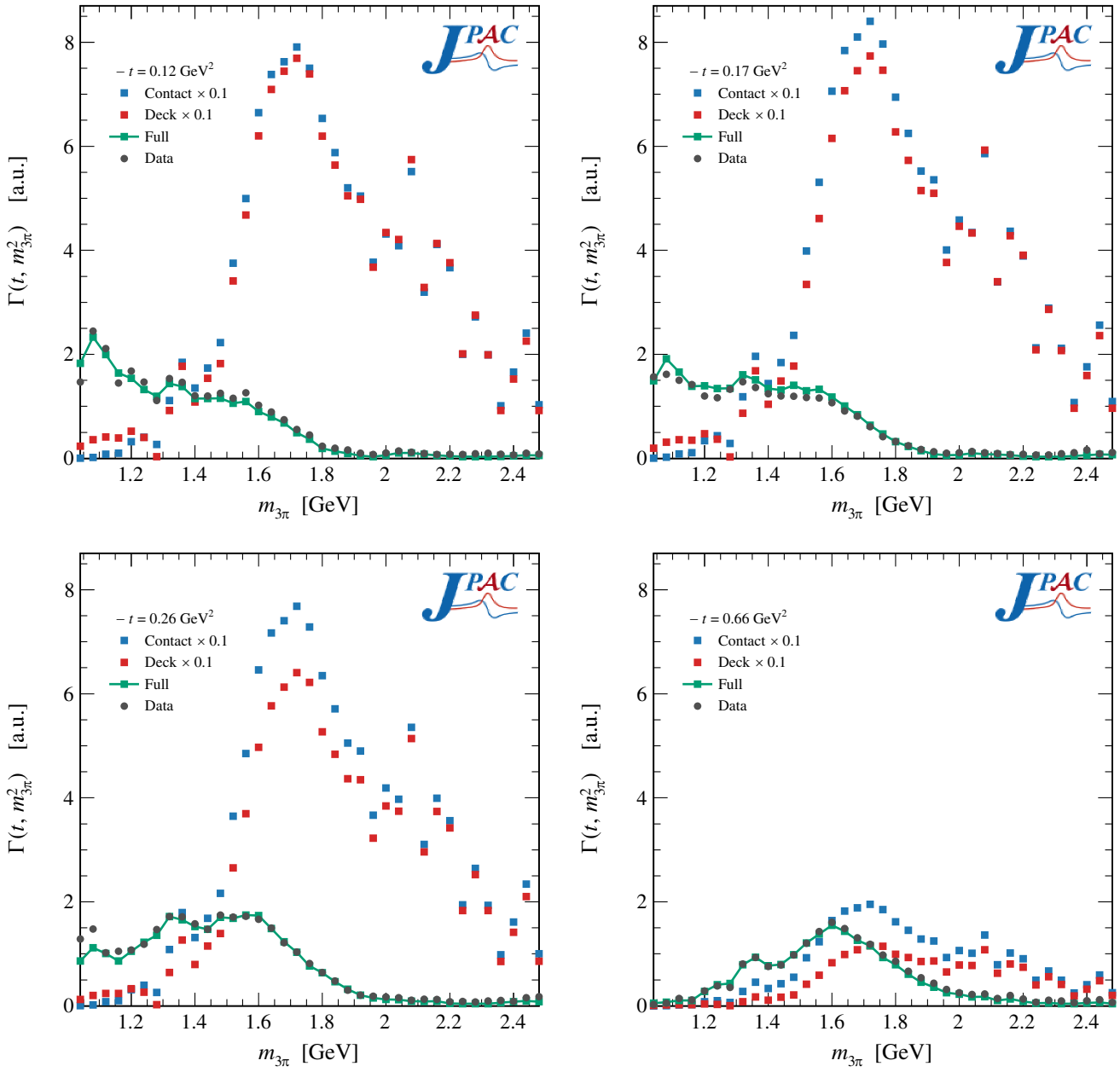


FIG. 13. Integrated intensity as a function of $m_{3\pi}$ compared to the COMPASS intensity. Unlike the t-dependence in Fig. 12, the $m_{3\pi}$-dependence is binned and thus we plot the bin centers connected by linear interpolations. As there is no explicit constraint of continuity, the line shape is purely the result of the data. Bootstrapped uncertainties are very small and thus we do not plot error bands.

V. SUMMARY AND OUTLOOK

In this work, we analyzed the COMPASS collaboration's free-isobar dataset relevant to the spin-exotic wave with $J^{PC} = 1^{-+}$. The experimental analysis assumes that the $\pi_1 \to 3\pi$ decay proceeds primarily via $\rho\pi$ in P wave, i.e., the so-called isobar approximation, and is thus decomposable into functions that parameterize individual $\pi\pi$ subchannels. This is the same dynamical assumption that enters the Khuri-Treiman formalism and makes the analysis readily comparable with dispersive models that are consistent with low-energy analyticity, unitarity, and crossing symmetry.

Because the π_1 is so wide, the effects of left-hand cut singularities from production processes must be taken into account to properly identify the exotic resonant signal. We outlined how the KT formalism can be extended to incorporate physics-motivated production amplitudes that replace the typical subtraction polynomials. With the COMPASS hadroproduction in mind, we explore solutions to the KT equations seeded by Born terms that are consistent with high-energy exchange and Regge phenomenology. These iterative solutions incorporate the ladder of $\rho\pi$ rescattering to all orders, as required by unitarity, and

yield the characteristic modifications to the ρ lines hape expected from different production amplitudes.

The unitarized isobars were used to perform a global fit to the COMPASS dataset, considering the full 3π Dalitz plots across production momentum transfer and three-body invariant mass simultaneously. This allows us to constrain the unknown line shapes that modify each production term as a function of $m_{3\pi}$ directly from the data, in a minimally model-dependent way. The result is a unitarized isobar model that describes the entire four-dimensional kinematic dependence of both production and decay variables. Notably, the 3π mass dependence revealed a surprisingly smooth distribution peaking at 1.6 GeV, suggestive of a possible spin-exotic resonance.

As discussed, to properly identify this line shape in the presence of such a resonance, one must be able to analytically continue the model into the complex plane and search for poles below the three-body cut. Such a continuation of the KT framework has been formally explored in the past [48], but, to our knowledge, has never been generalized beyond the S wave or implemented to extract a three-body resonance pole from data (analyses with similar approaches, however, include Refs. [88,89]). This analysis is the first step toward this goal, with the required continuation left as the focus of future work.

The unitarization of three-body production amplitudes within the isobar model presented in this analysis can also be readily adapted to other reactions of interest. The Deck mechanism, specifically, contributes to all partial waves explored by the freed-isobar analysis, and thus the driving terms presented here can be adapted to the analysis of any 3π decay by simply considering the appropriate analog of Eq. (12) for the projecting Lagrangian. This would allow the exploration of other members of the predicted hybrid multiplet, such as those in the 2^{-+} sector [90,91]. The three-body dynamics relevant to nonexotic decays are also of interest. The $a_1(1260)$, in particular, has recently been the subject of several studies [28,92–94], making a direct comparison with the COMPASS freed $1^{++}[\pi\pi]_{1^{--}}\pi$ S- and $1^{++}[\pi\pi]_{0^{++}}\pi$ P waves of timely interest.

The same can also apply to production effects relevant to 3π states in photo- or electroproduction processes studied at Jefferson Lab [95–97]. In these cases, the beam particle is a photon, and thus the exchange of a Reggeized charged π or ρ is expected to be the dominant production mechanism. These mechanisms have been argued to be enhanced relative to Pomeron exchange due to the hybrid nature of the π_1 [98–100]. The possibility of considering the $\pi_1^-\Delta^{++}$ final state may also enhance production cross sections, making photoproduction a promising avenue for spin-exotic searches in various decay modes [19,101] with the goal of understanding the properties of the elusive π_1.

The KT formalism has also been generalized to a number of hadronic decays to nonsymmetric final states, including $K\pi\pi$ [102–104], $\eta\pi\pi$ [82,105,106], and, more recently, $D\bar{D}K$ [107]. The methodology presented here may also be used to extend these analyses to production processes. This may become particularly important for investigations of three-body systems relevant to heavy exotic states, e.g., $J/\psi\pi\pi$ for both the $X(3872)$ and $Y(4260)$, at future collider facilities such as the EIC [108] and JLab22 [109].

ACKNOWLEDGMENTS

We thank Bastian Kubis for useful discussions and encouraging comments on early versions of the manuscript. We also thank the high-performance computing team of the Laboratorio de Modelos y Datos (LAMOD) at ICN-UNAM for their guidance with the TOCHTLI cluster which was used extensively in this work. This material is based upon work supported by the U.S. Department of Energy, Office of Science, Office of Nuclear Physics under Contract No. 89243126CSC000213, by U.S. Department of Energy Grant No. DE-FG02-87ER40365, and it contributes to the aims of the U.S. Department of Energy ExoHad Topical Collaboration, Contract No. DE-SC0023598. The work of S. G-S., G. M. and V. M. is supported by the Ministerio de Ciencia, Innovación y Universidades Grant No. PID2023-147112NB-C21, as well as through the award "Unit of Excellence María de Maeztu 2025-2029" to the Institute of Cosmos Sciences, Grant No. CEX2024-001451-M. S. G-S. also acknowledges additional support from the Generalitat de Catalunya (AGAUR) through Grant No. 2021SGR01095. S. G-S. is a Serra Húnter Fellow. V. M. is a Serra Húnter Professor. G. M. is a Beatriu de Pinós Fellow. We acknowledge financial support under the program "Progetti di Rilevante Interesse Nazionale" (PRIN 2022), published on 2.2.2022 by the Italian Ministry of University and Research (MUR), Project Title "The X (3872) files"—CUP J53C24002600006—Grant Assignment Decree No. 20429 adopted on 6.11.2024 by the Italian Ministry of University and Research (MUR).

DATA AVAILABILITY

Code to reproduce all results of this work are publicly available and can be found at [110,111].

APPENDIX A: DERIVATION OF ISOBAR DECOMPOSITION

The necessary structure of the isobar decomposition for an arbitrary decay $X_J \to 3\pi$ can be derived entirely from the crossing matrix (i.e., by requiring that the amplitude is crossing symmetric) and has been worked out in Ref. [59]. Here we briefly sketch the derivation for the π_1 case and refer to the reference above for more detailed discussion.

Because all particles involved are isovectors, the decay $\pi_1^i \to \pi^a\pi^b\pi^c$ for arbitrary isospin projections is related to that of $\pi_1^i\pi^{\bar{c}} \to \pi^a\pi^b$ and thus to a single scalar (reduced) amplitude by [we briefly show all three variables in Eq. (2) to better highlight symmetries]

$$\hat{\mathcal{F}}_{i\to abc}(\sigma_a,\sigma_b,\sigma_c) = \delta^{i\bar{c}}\delta^{ab}\hat{\mathcal{F}}(\sigma_a,\sigma_b,\sigma_c) + \delta^{ib}\delta^{a\bar{c}}\hat{\mathcal{F}}(\sigma_c,\sigma_a,\sigma_b) + \delta^{ia}\delta^{b\bar{c}}\hat{\mathcal{F}}(\sigma_b,\sigma_c,\sigma_a). \tag{A1}$$

Alternatively, Eq. (A1) can be written in terms of isospin-projectors and amplitudes of definite isospin, $\hat{\mathcal{F}}^I$, in the c-frame (i.e., the center-of-mass frame for the $i\bar{c}\to ab$ reaction). These isospin amplitudes are related to the scalar amplitude by,

$$\begin{bmatrix}\hat{\mathcal{F}}(\sigma_a,\sigma_b,\sigma_c)\\ \hat{\mathcal{F}}(\sigma_b,\sigma_c,\sigma_a)\\ \hat{\mathcal{F}}(\sigma_c,\sigma_a,\sigma_b)\end{bmatrix} = \frac{1}{6}\begin{bmatrix}2 & 0 & -2\\ 0 & 3 & 3\\ 0 & -3 & 3\end{bmatrix}\begin{bmatrix}\hat{\mathcal{F}}^0(\sigma_a,\sigma_b,\sigma_c)\\ \hat{\mathcal{F}}^1(\sigma_a,\sigma_b,\sigma_c)\\ \hat{\mathcal{F}}^2(\sigma_a,\sigma_b,\sigma_c)\end{bmatrix}. \tag{A2}$$

Each amplitude on the right-hand side can be expanded into isospin partial waves as,

$$\hat{\mathcal{F}}^I(\sigma_a,\sigma_b,\sigma_c) = \sum_{j=1}^{\infty}\kappa_c^{j-1}P'_j(z_c)\hat{f}^I_j(\sigma_c), \tag{A3}$$

where a $j=0$ term is prohibited due to the transversity of the π_1 which also yields angular structure in terms of the first derivative of the Legendre polynomials. The c-frame scattering angle is related to the crossed channel decay variables by,

$$z_c = \frac{\sigma_b-\sigma_a}{\kappa_c}, \tag{A4a}$$

with

$$\kappa_c^2 = \kappa^2(\sigma_c) = (1-\sigma_{\rm th}/\sigma_c)(p_{\rm th}-\sigma_c)(r_{\rm th}-\sigma_c), \tag{A4b}$$

denoting the Kacser function [112] in terms of the 2π threshold $\sigma_{\rm th}=4\mu^2$ and the "regular" and "pseudo"-thresholds of the scattering reaction: $r_{\rm th}=(m_{3\pi}+\mu)^2$ and $p_{\rm th}=(m_{3\pi}-\mu)^2$, respectively. Prefactors of κ are the angular momentum barrier factors and are included in Eq. (A3) such that it is free from kinematic singularities.

The isobar model assumption then amounts to truncating Eq. (A3) to a finite $j_{\rm max}$, replacing $\hat{f}^I_j(\sigma)$ with isobars $F^I_j(\sigma)$ and, to reinstate crossing symmetry, adding analogous truncated expansions corresponding to the projections of the a- and b channels. These crossed channel terms must enter with the appropriate Wigner matrices to rotate both the helicity and isospin projections back onto the c channel [113]. Luckily, the crossing structure of natural-parity vector decays is trivial and the general isobar decomposition reads,

$$\hat{\mathcal{F}}^I(\sigma_a,\sigma_b,\sigma_c) = 2\sum_{j=1}^{j_{\rm max}}\Big\{\kappa_c^{j-1}P'_j(z_c)F^I_j(\sigma_c) - \sum_{I'}C_{II'}[\kappa_b^{j-1}P'_j(z_b)F^{I'}_j(\sigma_b) + (-1)^{I+I'}\kappa_a^{j-1}P'_j(z_a)F^{I'}_j(\sigma_a)]\Big\}, \tag{A5}$$

where the isospin crossing matrix is

$$C_{II'} = \begin{bmatrix}\frac{1}{3} & 1 & \frac{5}{3}\\ \frac{1}{3} & \frac{1}{2} & -\frac{5}{6}\\ \frac{1}{3} & -\frac{1}{2} & \frac{1}{6}\end{bmatrix}, \tag{A6}$$

and the crossed channel κ and z given by Eq. (A4) with the appropriate interchange of $c\leftrightarrow b$ or $c\leftrightarrow a$. A factor of 2 is also included in the normalization for convenience to remove overall factors in the final expression.

As a final step, at small values of σ (e.g., within the physical decay region), the barrier factors will suppress contributions from higher spin and we truncate to $j_{\rm max}=1$. Bose symmetry will thus enforce that the only relevant isobar will be $F^1_1(\sigma)$ in each channel. Inserting Eq. (A5) with this truncation into Eq. (A2), yields the final decomposition of Eq. (5).

APPENDIX B: $\boldsymbol{\Delta(t,m_{3\pi}^2;\sigma)}$ AND ITS ANALYTIC CONTINUATION

The discontinuity of the Deck triangle diagram in Eq. (22) is best written in terms of s-channel center-of-mass frame variables of the $\pi\mathbb{P}\to\pi\rho$ reaction. To this end, we write the (moduli of) incoming and outgoing momenta as,

$$|\boldsymbol{k}| = \frac{\sqrt{\lambda(m_{3\pi}^2,t,\mu^2)}}{2m_{3\pi}}, \qquad |\boldsymbol{q}| = \frac{\sqrt{\lambda(m_{3\pi}^2,\sigma,\mu^2)}}{2m_{3\pi}}, \tag{B1}$$

in terms of the usual Källén triangle function [114]. We note that the "initial state" Pomeron is spacelike and thus $t\le 0$, but, because both $|\boldsymbol{k}|$ and $|\boldsymbol{q}|$ have straightforward analytic continuations, this poses no problems. We may also define the kinematic phase space factor of the $\rho\pi$ system in P wave,

$$\rho_{\pi\rho P} = \frac{2|\boldsymbol{q}|^3}{m_{3\pi}}, \tag{B2}$$

which we emphasize is a function of (and can be continued to arbitrary complex values of) both the total center-of-mass energy and floating ρ mass, i.e., $m_{3\pi}$ and σ, respectively.

From Fig. 1, the exchanged pion enters as a pole in the momentum transfer between the beam pion and ρ, which

can be written in terms of Eq. (B1) and a new scattering angle as,

$$\tau(z) = \mu^2 + \sigma - \frac{(m_{3\pi}^2 + \mu^2 - t)(m_{3\pi}^2 - \mu^2 + \sigma)}{2m_{3\pi}^2} + 2|\boldsymbol{q}||\boldsymbol{k}|z. \tag{B3}$$

Projecting this pole onto the P wave yields Eq. (22) in terms of the Legendre function of the second kind, $Q_0(\zeta)$, with argument [81]

$$\zeta = \frac{1}{2|\boldsymbol{q}||\boldsymbol{k}|}[\mu^2 - \tau(0)]. \tag{B4}$$

The Legendre functions of the second kind have a straightforward analytic continuation to arbitrary values of Eq. (B4) [115]. We note that Q_0 (and therefore Δ) develops an imaginary part at $\sigma < 0$ corresponding to the left-hand cut which emerges when projecting the crossed channel exchanges onto the s channel.

In addition, for certain kinematics, the Q_0 may also develop a complex cut on for $\mathrm{Re}\,\sigma > 0$. Such a right-hand cut is an kinematical artifact of the partial-wave projection and does not correspond to the opening of a multibody threshold. As a result, it may always be avoided by a suitable analytical continuation. The branch point corresponding to $|\zeta| = 1$ in the right-half complex σ plane, however, will manifest as a pinch-singularity which must be treated with care, see, e.g., discussion in Ref. [66]. Luckily, in the kinematics considered in this work, these complications are sufficiently far from the physical region (and path of integration required by solutions to KT) and thus do not need to be treated explicitly.

As discussed in Sec. II B, Δ corresponds to the discontinuity of the Feynman loop Eq. (18a). In fact, it is analytic for real $m_{3\pi}$ (and physical $2\mu \leq \sqrt{\sigma} \leq m_{3\pi} - \mu$) and, because $t \leq 0$, the only intermediate state that contributes to the loop is that of $m_{3\pi}$ and thus it can be entirely reconstructed by dispersing (with the phase space),

$$\hat{\mathcal{T}}(t, m_{3\pi}^2; \sigma) = \hat{\mathcal{T}}(t, 0; \sigma) + \frac{m_{3\pi}^2}{\pi}\int_{(\sqrt{\sigma}+\mu)^2}^{\infty} \frac{dx}{x}\frac{\rho_{\pi\rho P}\Delta(t, x; \sigma)}{x - m_{3\pi}^2}. \tag{B5}$$

This implies that $\mathrm{Im}\,\hat{\mathcal{T}}(t, m_{3\pi}^2; \sigma) = \rho_{\pi\rho P}\Delta(t, m_{3\pi}^2; \sigma)$ within the Dalitz region. These two will deviate for unphysical σ where the discontinuity itself becomes complex.

APPENDIX C: OTHER PRODUCTION DIAGRAMS

In this appendix, we discuss other production diagrams which can be considered in addition to the contact and Deck production processes in Secs. II A and II B but are ignored in our analysis. These effectively fall into three categories: Deck-like processes with heavier exchanges, nucleon spin-flip diagrams, and non-Pomeron exchanges.

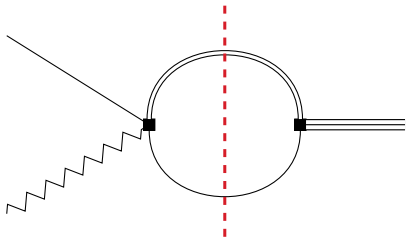


FIG. 14. Bubble diagram emerging from heavier Deck-like diagrams. The heavier exchange propagator can be shrunk to contact $\pi\pi\rho\mathbb{P}$ interaction resulting in an effective bubble diagram.

The first class of production diagrams include Deck-like mechanisms involving the exchange of heavier particles. These arise from the production via ρ/f_2 exchange, inclusion of a form factor, or Reggeization effects of the pion pole at large $m_{3\pi}^2$ [116].

Naïvely replacing $\mu \to \Lambda$ in Eq. (16) causes the amplitude to vanish asymptotically as $\Lambda \to \infty$ (at fixed $m_{3\pi}$). This is because increasing the exchanged mass moves the logarithmic singularity contained in $Q_0(\zeta)$ farther from the Dalitz region [117]. We may thus reasonably expect a hierarchy in which the lightest exchange (i.e., the pion exchange in Sec. II B) is the most influential for the amplitude line shape, while the effects of heavier exchanges are smoother and therefore can be absorbed into the normalizations of the contact or Deck terms.

To investigate the effect of finite Λ, we may simply expand the vertical propagator in the Deck loop integrand and ignore momenta with $\ell^2 > \Lambda^2$,

$$\frac{1}{\Lambda^2 - \ell^2} = \frac{1}{\Lambda^2}\left[1 + \mathcal{O}\left(\frac{\ell^2}{\Lambda^2}\right)\right]. \tag{C1}$$

This effectively shrinks the triangle diagram in Fig. 3 to a bubble, as shown in Fig. 14, and thus instead of Eq. (20) we arrive at,

$$\mathcal{T}(t, m_{3\pi}^2; \sigma) \approx [\epsilon_{\mu\nu\alpha\beta}\pi_1^\mu k^\nu q^\alpha \mathbb{P}^\beta] \times \Lambda^{-2}\hat{\mathcal{B}}(m_{3\pi}^2; \sigma), \tag{C2}$$

with $\hat{\mathcal{B}}$ a scalar, logarithmically divergent two-point integral.[14] Proceeding as in Sec. II B, we cut the loop and note that

$$\frac{1}{2i}[\hat{\mathcal{B}}(m_{3\pi}^2 + i\epsilon; \sigma) - \hat{\mathcal{B}}(m_{3\pi}^2 - i\epsilon; \sigma)] = \rho_{\pi\rho P}. \tag{C3}$$

[14]Again, in the notation of LoopTools, $\hat{\mathcal{B}}(m_{3\pi}^2; \sigma) = (4/\pi)B_{00}(m_{3\pi}^2, \sigma, \mu^2)$.

This means that after removing the phase space factor, we are left with a constant and thus these diagrams are indistinguishable from the contact term of Eq. (12) to first order.

The second class of diagrams beyond those considered in the main text include nucleon spin-flip interactions at the bottom vertex. The effect of such interactions arises from Eq. (14) where we may consider $|\lambda - \lambda'| = 1$. This would permit us to add a second copy of either B_{Contact} or B_{Deck} with an additional factor of $\sqrt{-t}$ and a different normalization. In principle, such a term would be required to describe the large-t kinematics where spin-flip contributions are expected to dominate, but are unnecessary for the current dataset with $t < 1$ GeV^2.

Finally, Regge exchanges other than the Pomeron are also possible in the bottom vertex (i.e., exchanged with the target), such as those involving the ρ or f_2 trajectories. These meson exchanges will all have Regge intercepts less than unity and thus will be asymptotically suppressed relative to the Pomeron as $s \to \infty$ [61,74]. At finite kinematics, however, these diagrams may still have a non-negligible effect—especially in high-statistics analyses. For instance, f_2 exchange with the nucleon has recently been shown to be necessary to accurately describe the momentum-transfer distribution of $\eta^{(\prime)}\pi$ pairs [118–121], contradicting the typical assumption that the full range of COMPASS kinematics requires only Pomeron exchange.

In our current application, both Deck and contact production can proceed via a subleading meson exchange. The primary effect of considering such a diagram enters through the amplitude's total s dependence, e.g., through the $s^{\alpha(t)}$ factor in Eq. (13). Since we are not sensitive to this dependence, swapping the Pomeron for any other Reggeon simply adds functionally identical copies of the production term with different parameters. For example, contactlike production mediated by ρ exchange is included by adding a second Eq. (15) with different parameters. If the parameters of both ρ and $\mathbb{P}$ diagrams are *a priori* unknown and to be determined by fit, it will not be possible to unambiguously identify which term corresponds to which exchange. Therefore, we will generally continue to assume Pomeron dominance so that we may focus on comparing different top vertex dynamics.

APPENDIX D: THE $\sigma \to \infty$ LIMIT AND DOUBLE REGGE ASYMPTOTICS

In order to determine the number of subtractions needed in Eq. (29), one typically considers the properties of the isobars in the $\sigma \to \infty$ limit. Specifically, as the power m governs the asymptotic behavior of the rescattering term, it is customarily assumed to match the leading power in the homogeneous solution in Eq. (10). If $B(t, m_{3\pi}^2; \sigma \to \infty) \propto \sigma^i$, then, we choose the number of subtractions to be $m = i + 1$ so that the inhomogeneous term is asymptotically of the same order. When multiplied by the Omnès function, if the phase shift asymptotically approaches $\delta(\sigma \to \infty) = k\pi$ for integer k,[15] the full isobar will go as $F_B(t, m_{3\pi}^2; \sigma \to \infty) \propto \sigma^{i-k}$. Although this fixed-power scaling is unphysical for any i and k [123], their values are still chosen to at least minimize violations of high-energy expectations, such as the Froissart bound [124].

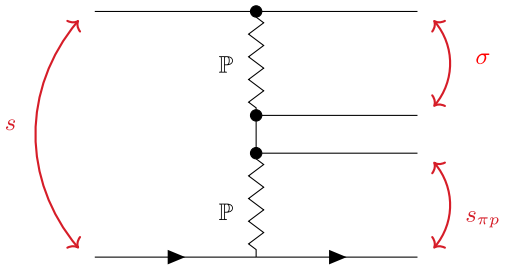


FIG. 15. "Fast-π" diagram of Deck-like production in the double Regge limit. The invariant mass of the centrally produced $\pi\pi$ system is assumed to be small compared to σ and $s_{\pi p}$ such that the middle pion exchange does not Reggeize.

Because the $\rho\pi$ system is embedded in a production amplitude with Regge kinematics, one should, in principle, consider the effect of bottom $\mathbb{P}$ exchange when taking $\sigma \to \infty$. Specifically, if $s > m_{3\pi}^2 > \sigma$ and $s_{\pi p}$ are all large, the reaction will resemble central $\pi\pi$ production, with both the beam and target diffracting, i.e., exchanging a Pomeron, as in Fig. 15. Such "double Regge" processes are being investigated in $\eta^{(\prime)}\pi$ production relevant for the π_1 at COMPASS [15,118] and at GlueX [125,126].

Avoiding unphysical overlapping singularities in the 3π and $\pi\pi p$ channels imposes very nontrivial constraints on the possible σ dependence required by analyticity in the double Regge limit [127]. Taking $\tau = t \approx 0$ (cf., Fig. 1), the leading σ behavior will be the same for diagrams in which the final state π or $\pi\pi$ system are the "fast particle" (i.e., travel in the beam direction) and yield

$$\mathcal{F}(t, m_{3\pi}^2; \sigma \to \infty, \sigma') \propto \sigma^{\alpha_{\mathbb{P}}(0) - \alpha_{\mathbb{P}}(0)} = \sigma^0. \quad \text{(D1)}$$

This bound is more constraining than the naive single Regge limit where one ignores that the bottom Pomeron exchange is already Reggeized, i.e., $\sigma^{\alpha_{\mathbb{P}}(0)} \approx \sigma^1$. In order to satisfy the upper bound set by Eq. (D1), we should expect

[15]As our model is only constrained by elastic unitarity, the extrapolation of the $\delta(\sigma)$ beyond a few GeV (and therefore the choice of k) is largely arbitrary. We follow Ref. [39] and match the constrained fits to data (CFD) result of Ref. [122] to the form,

$$\delta(s > s_m) = \pi - \frac{a}{b + (s/s_m)^{3/2}},$$

where a and b are chosen to smoothly match $\delta(s_m)$ and $\delta'(s_m)$ at $s_m = 1.3$ GeV^2.

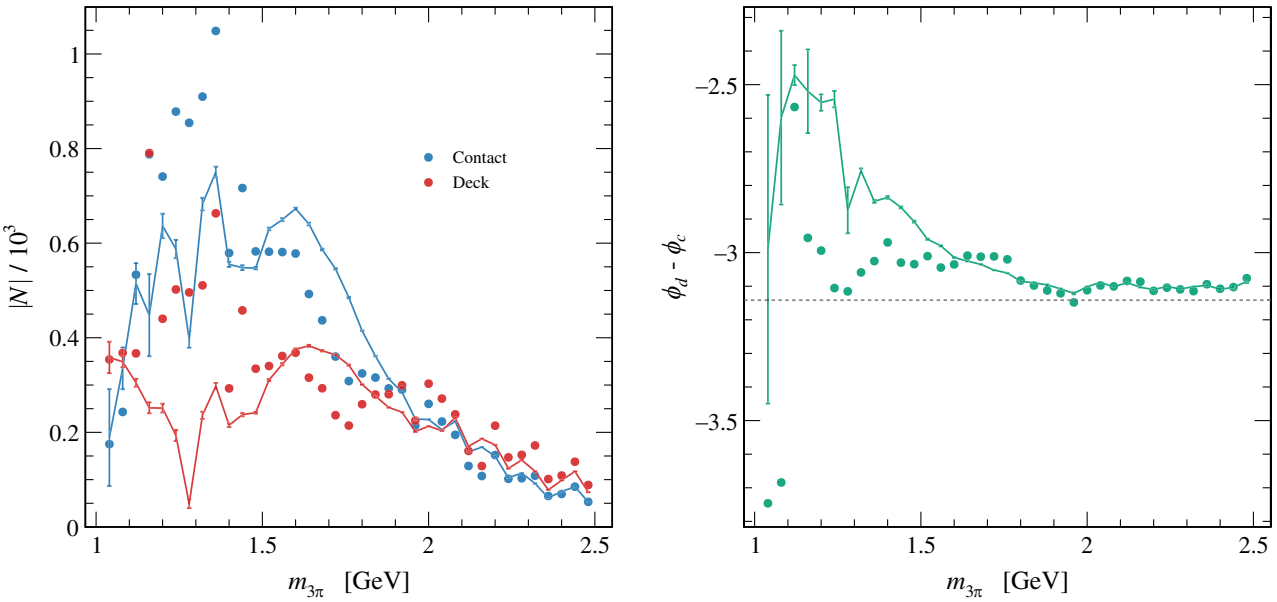


FIG. 16. $|N_c|$ and $|N_d|$ distributions (left) and phase difference (right) resulting from the extended fit. For comparison, we superimpose linear interpolations of the distributions from the minimal model (i.e., Fig. 10) as solid curves.

our isobars to be asymptotically bounded by σ^{-1} in order to counteract the Kibble factor in Eq. (3). With a standard parametrization of the P-wave $\pi\pi$ phase shift [122] extrapolated to $\delta(\sigma \to \infty) = \pi$, this limit is saturated by the contact and Deck driving terms of Secs. II A and II B, respectively, with $m = 1$.

It is important to note that unlike the contact term, the Deck contribution can introduce arbitrary polynomials of σ by considering non-minimal vertices with derivatives in the Feynman loop of Fig. 3. Any such coupling will, however, exceed the bound imposed by Eq. (D1) and thus violate high-energy unitarity and analyticity.

APPENDIX E: FITTING A THIRD t SLOPE

The global fit results of Sec. IV suggest a possibility of production effects beyond those present in the nominal contact-plus-Deck model. Specifically, the region of small $m_{3\pi}$ is seen to be systematically less well described as the higher mass tail and coincides with the observation of a steeper characteristic t-slope in Ref. [33]. This may point to contributions of subleading nucleon spin-flip or non-Pomeron exchange diagrams (cf. Appendix C).

To gauge whether this is the case, here, we consider fits with a nonminimal t dependence by introducing an additional contact term. We make the replacement,

$$N_c(m_{3\pi}^2)e^{ct} \to N_c(m_{3\pi}^2)e^{ct} + N_c'(m_{3\pi}^2)e^{c't}, \quad \text{(E1)}$$

in terms of a third t slope and set of normalizations. We assume this new term to have the same phase as the original contact term (i.e., $\phi_c' = 0$), so as to not overproliferate the number of free parameters but still allow interference with the Deck term.

The resulting binwise parameters and χ^2 distributions are plotted in Figs. 16–18. The best-fit values of t slopes for the original contact and Deck terms are

$$c = 2.78\ \text{GeV}^{-2} \quad \text{and} \quad d = 2.91\ \text{GeV}^{-2}, \quad \text{(E2)}$$

which are roughly comparable with the values seen in Eq. (40), while the new contact term has a steeper t

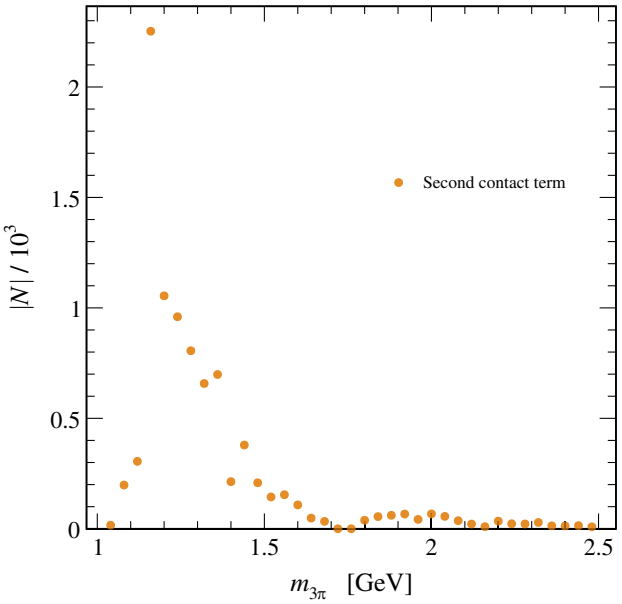


FIG. 17. Binwise distributions of the second contact term in the extended fit.

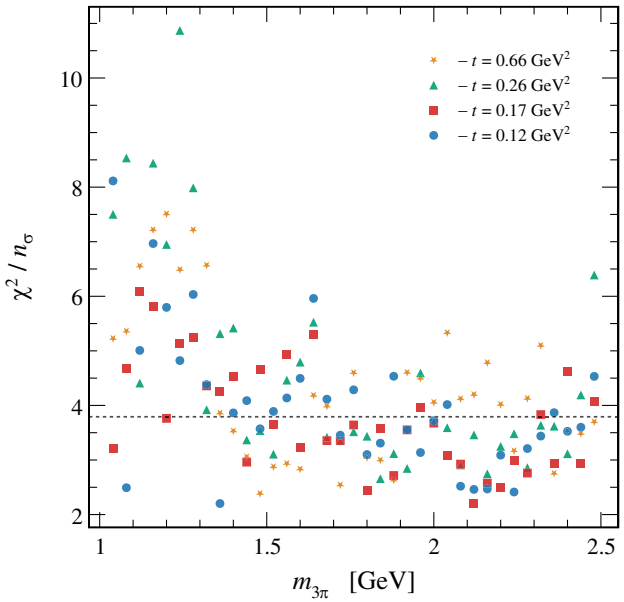


FIG. 18. Distribution of normalized χ^2's resulting from the extended model. The dashed line denotes the $\chi^2/\text{d.o.f.} = 3.80$.

dependence with $c' = 5.66\ \text{GeV}^{-2}$. Examining the N'_c distribution, this term indeed contributes primarily in the $m_{3\pi} < 1.5$ GeV region, as expected, while the N_c and N_d distributions now have a milder $m_{3\pi}$ dependence with a less obvious peak at 1.6 GeV when compared to Fig. 10. The phase difference of the new fit also now hovers around $-\pi$ throughout the entire energy range indicating all normalizations are approximately real with purely destructive interference. We note that, because of this interference, the lack of as obvious of a peak in the normalizations does not indicate the absence of a resonance, since the final line shape in the small mass region is determined by possible cancellations between individual amplitudes. This result also validates the increase of $\text{Im}\,N_d$ observed in the minimal fit as driven by the different interference pattern needed to account for the steeper t-dependence at small 3π masses.

The quantitative improvement of the fit quality, however, is relatively little. The extended fit results in a $\bar{\chi}^2 = 4.15$ and a $\chi^2/\text{d.o.f.} = 3.79$ which is less than a 10% difference over the quoted results of Sec. IV. Examining the bin-by-bin distribution of χ^2's in Fig. 18, we see a very similar distribution as Fig. 11 with systematically larger χ^2/n_σ in the small $m^2_{3\pi}$ bins. This suggests that, while the inclusion of additional t-dependence allows small (likely overfitted) improvements throughout the entire energy range, it does not address the primary deficiency of the current description in the low mass region. As such, we will continue to quote the minimal contact-plus-Deck model as our primary result with the caveat that the extracted parameter distributions are still subject to deviations based on the model considered. Ultimately how much these changes affect an extraction of the π_1 pole will need to be taken into account in the uncertainty analysis of any future work.

APPENDIX F: BOOTSTRAP ANALYSIS

The uncertainties in the fit parameters are determined as the standard deviation of parameter distributions resulting from 10^4 bootstrap samples. Because the quoted experimental uncertainties are so small, doing a traditional bootstrap analysis, i.e., assuming each parameter is uncorrelated and generating pseudodata of each data point within its Gaussian error, produces tiny, sub-1% uncertainties in all parameters. This is clearly unrealistic, especially considering the size of the pull and χ^2 distributions in Figs. 9 and 11.

Instead, for each data point $\mathcal{F}_k^{\text{ex}}$ corresponding to the four-dimensional intensity, we calculate,

$$S_k = \left| \frac{|\mathcal{F}_k^{\text{ex}}| - |\mathcal{F}_k^{\text{BF}}|}{\delta|\mathcal{F}_k^{\text{ex}}|} \right|, \tag{F1}$$

where $|\mathcal{F}_k^{\text{BF}}|$ is the best-fit model curve evaluated at the same kinematic point. Clearly Eq. (F1) corresponds to absolute value of the pull calculated from the best-fit curve with $\chi^2 = \sum_k S_k^2$. If $S_k \geq 1$, bootstrap pseudodata are resampled within a Gaussian of width $S_k\sigma_k$ otherwise the original experimental uncertainty σ_k is used. The bootstrapped data then is fit with Eq. (36) as before with the original errors. This procedure scales the spread of data points by their local distance to the best-fit curve and thus is expected to capture a slightly more realistic estimation of parameter uncertainties.

The resulting $\bar{\chi}^2$ distribution of the global fit is plotted in Fig. 19, where we indeed see a Gaussian-like distribution with a mean approximately at twice the best-fit value. Example parameter distributions, e.g., for $|N_c|$, are also

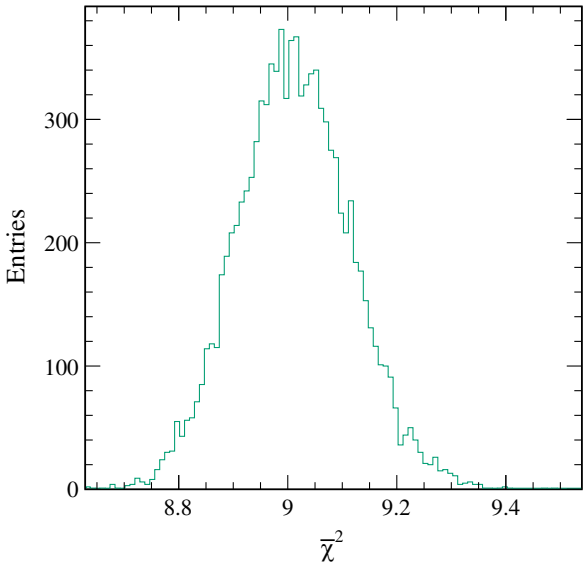


FIG. 19. Bootstrapped distributions of the fit function $\bar{\chi}^2$ for the global fits.

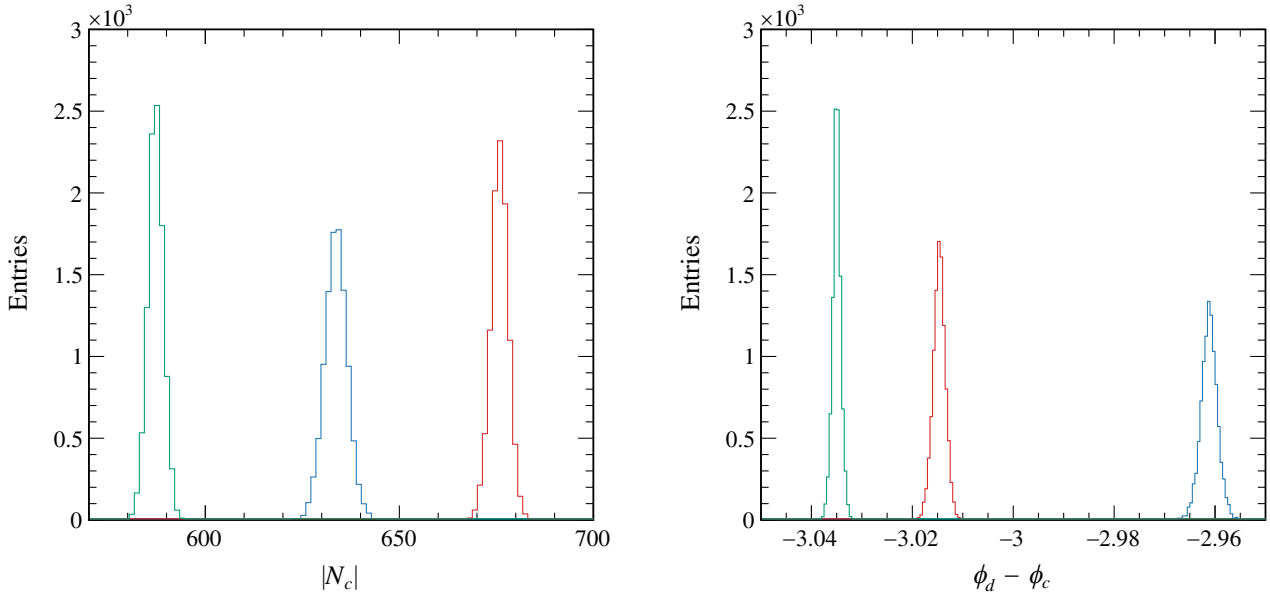


FIG. 20. Bootstrapped distributions of the $|N_c|$ (left) and the phase difference (right) at fixed values of $m_{3\pi} = 1.52$ (blue), 1.6 (red), and 1.68 GeV (green).

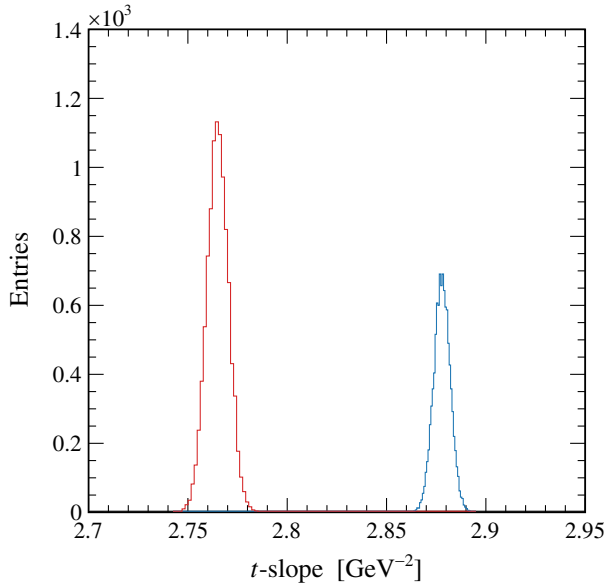


FIG. 21. Bootstrapped distributions of the t-slope for the contact c (blue) and Deck d (red) terms.

plotted in Fig. 20 and those of the t slopes in Fig. 21. Despite such a multidimensional fit, all normalization and phase parameters appear fairly Gaussian-like, without nearby local minima, and therefore allow straightforward calculations of the 1σ uncertainty. This likely reflects the relatively uncorrelated nature of the binwise normalizations of the different terms.

We note that the bin-by-bin correlations of the COMPASS isobars do not explicitly factor into Eq. (F1). These correlations are used in the original calculation of the data uncertainty (as detailed in Sec. IV) but are much smaller than the effect of rescaling by an average of $\bar{S}_k = \sqrt{\bar{\chi}^2} \approx 2$,[16] and thus ignored in the bootstrap resampling. The correlations will still enter implicitly as systematically shifted points are assumed to have a similarly correlated distance to the smooth best-fit curve.

In the end, despite the rescaling, the estimated uncertainties remain very small and possibly still a severe underestimation of the true values. We remind that this smallness is related to the lack of systematic error estimation in the experimental freed-isobar analysis at present. As such, our parameter uncertainties are likely a reliable estimation of the relative error but will require further scaling in their absolute size in any subsequent analysis.

[16]To check consistency, we conducted the original fit including correlations with all errors inflated by a global factor of $\sqrt{\bar{\chi}^2}$, which indeed yields $\chi^2/\text{d.o.f.} \approx 1$.

[1] D. R. Thompson *et al.* (E852 Collaboration), Phys. Rev. Lett. **79**, 1630 (1997).
[2] S. U. Chung *et al.* (E852 Collaboration), Phys. Rev. D **60**, 092001 (1999).
[3] G. S. Adams *et al.* (E862 Collaboration), Phys. Lett. B **657**, 27 (2007).
[4] A. Abele *et al.* (Crystal Barrel Collaboration), Phys. Lett. B **423**, 175 (1998).
[5] E. I. Ivanov *et al.* (E852 Collaboration), Phys. Rev. Lett. **86**, 3977 (2001).
[6] Y. A. Khokhlov (VES Collaboration), Nucl. Phys. **A663**, 596 (2000).
[7] D. Horn and J. Mandula, Phys. Rev. D **17**, 898 (1978).
[8] N. Isgur and J. E. Paton, Phys. Rev. D **31**, 2910 (1985).
[9] M. S. Chanowitz and S. R. Sharpe, Nucl. Phys. **B222**, 211 (1983); **B228**, 588(E) (1983).
[10] T. Barnes, F. E. Close, and F. de Viron, Nucl. Phys. **B224**, 241 (1983).
[11] J. J. Dudek, R. G. Edwards, P. Guo, and C. E. Thomas (Hadron Spectrum Collaboration), Phys. Rev. D **88**, 094505 (2013).
[12] A. J. Woss, J. J. Dudek, R. G. Edwards, C. E. Thomas, and D. J. Wilson (Hadron Spectrum Collaboration), Phys. Rev. D **103**, 054502 (2021).
[13] C. A. Meyer and Y. Van Haarlem, Phys. Rev. C **82**, 025208 (2010).
[14] C. A. Meyer and E. S. Swanson, Prog. Part. Nucl. Phys. **82**, 21 (2015).
[15] C. Adolph *et al.* (COMPASS Collaboration), Phys. Lett. B **740**, 303 (2015); **811**, 135913(E) (2020).
[16] A. Rodas *et al.* (JPAC Collaboration), Phys. Rev. Lett. **122**, 042002 (2019).
[17] M. Albrecht *et al.* (Crystal Barrel Collaboration), Eur. Phys. J. C **80**, 453 (2020).
[18] B. Kopf, M. Albrecht, H. Koch, M. Küßner, J. Pychy, X. Qin, and U. Wiedner, Eur. Phys. J. C **81**, 1056 (2021).
[19] F. Afzal *et al.* (GlueX Collaboration), Phys. Rev. Lett. **133**, 261903 (2024).
[20] M. Mai and M. Doring, Phys. Rev. Lett. **122**, 062503 (2019).
[21] R. A. Briceño, M. T. Hansen, A. W. Jackura, R. G. Edwards, and C. E. Thomas, arXiv:2510.24894.
[22] M. T. Hansen, R. A. Briceño, R. G. Edwards, C. E. Thomas, and D. J. Wilson (Hadron Spectrum Collaboration), Phys. Rev. Lett. **126**, 012001 (2021).
[23] T. D. Blanton, F. Romero-López, and S. R. Sharpe, Phys. Rev. Lett. **124**, 032001 (2020).
[24] M. Fischer, B. Kostrzewa, L. Liu, F. Romero-López, M. Ueding, and C. Urbach, Eur. Phys. J. C **81**, 436 (2021).
[25] S. M. Dawid, Z. T. Draper, A. D. Hanlon, B. Hörz, C. Morningstar, F. Romero-López, S. R. Sharpe, and S. Skinner, Phys. Rev. D **112**, 014505 (2025).
[26] H. Yan, M. Mai, M. Garofalo, U.-G. Meißner, C. Liu, L. Liu, and C. Urbach, Phys. Rev. Lett. **133**, 211906 (2024).
[27] H. Yan, M. Mai, M. Garofalo, Y. Feng, M. Döring, C. Liu, L. Liu, U.-G. Meißner, and C. Urbach, arXiv:2510.09476.
[28] M. Mai, A. Alexandru, R. Brett, C. Culver, M. Döring, F. X. Lee, and D. Sadasivan (GWQCD Collaboration), Phys. Rev. Lett. **127**, 222001 (2021).
[29] C. Culver, M. Mai, R. Brett, A. Alexandru, and M. Döring, Phys. Rev. D **101**, 114507 (2020).
[30] A. W. Jackura, Phys. Rev. D **108**, 034505 (2023).
[31] A. W. Jackura, S. M. Dawid, C. Fernández-Ramírez, V. Mathieu, M. Mikhasenko, A. Pilloni, S. R. Sharpe, and A. P. Szczepaniak, Phys. Rev. D **100**, 034508 (2019).
[32] B. Ketzer, B. Grube, and D. Ryabchikov, Prog. Part. Nucl. Phys. **113**, 103755 (2020); **128**, 104000(E) (2023).
[33] C. Adolph *et al.* (COMPASS Collaboration), Phys. Rev. D **95**, 032004 (2017).
[34] F. Krinner, D. Greenwald, D. Ryabchikov, B. Grube, and S. Paul, Phys. Rev. D **97**, 114008 (2018).
[35] F. Krinner, Freed-isobar partial-wave analysis, Ph.D. thesis, Munich, Tech. U., 2018.
[36] M. G. Alexeev *et al.* (COMPASS Collaboration), Phys. Rev. D **105**, 012005 (2022).
[37] N. N. Khuri and S. B. Treiman, Phys. Rev. **119**, 1115 (1960).
[38] P. Guo, I. V. Danilkin, C. Fernández-Ramírez, V. Mathieu, and A. P. Szczepaniak, Phys. Lett. B **771**, 497 (2017).
[39] I. V. Danilkin, C. Fernández-Ramírez, P. Guo, V. Mathieu, D. Schott, M. Shi, and A. P. Szczepaniak, Phys. Rev. D **91**, 094029 (2015).
[40] F. Niecknig, B. Kubis, and S. P. Schneider, Eur. Phys. J. C **72**, 2014 (2012).
[41] A. Garcia-Lorenzo, M. Albaladejo, S. Gonzlez-Solis, N. Hammoud, V. Mathieu, G. Montana, A. Pilloni, D. Winney, and A. P. Szczepaniak (JPAC Collaboration), arXiv:2505.15309.
[42] V. Bernard, S. Descotes-Genon, M. Knecht, and B. Moussallam, Eur. Phys. J. C **84**, 744 (2024).
[43] M. Albaladejo *et al.* (JPAC Collaboration), Phys. Rev. D **108**, 014035 (2023).
[44] M. Albaladejo, I. Danilkin, S. Gonzalez-Solis, D. Winney, C. Fernandez-Ramirez, A. N. H. Blin, V. Mathieu, M. Mikhasenko, A. Pilloni, and A. Szczepaniak (JPAC Collaboration), Eur. Phys. J. C **80**, 1107 (2020).
[45] G. Colangelo, S. Lanz, H. Leutwyler, and E. Passemar, Eur. Phys. J. C **78**, 947 (2018).
[46] X.-H. Cao, F.-K. Guo, C. Hanhart, and B. Kubis, arXiv:2512.00501.
[47] H. Akdag, B. Kubis, and A. Wirzba, J. High Energy Phys. 03 (2023) 059.
[48] I. J. R. Aitchison and R. Pasquier, Phys. Rev. **152**, 1274 (1966).
[49] I. J. R. Aitchison, J. Phys. G **3**, 121 (1977).
[50] R. Pasquier and J. Y. Pasquier, Phys. Rev. **170**, 1294 (1968).
[51] R. Pasquier and J. Y. Pasquier, Phys. Rev. **177**, 2482 (1969).
[52] M. Mikhasenko, Y. Wunderlich, A. Jackura, V. Mathieu, A. Pilloni, B. Ketzer, and A. P. Szczepaniak, J. High Energy Phys. 08 (2019) 080.
[53] D. Stamen, T. Isken, B. Kubis, M. Mikhasenko, and M. Niehus, Eur. Phys. J. C **83**, 510 (2023); **83**, 586(E) (2023).
[54] R. T. Deck, Phys. Rev. Lett. **13**, 169 (1964).
[55] G. Ascoli, L. M. Jones, B. Weinstein, and H. W. Wyld, Phys. Rev. D **8**, 3894 (1973).
[56] G. Ascoli, R. Cutler, L. M. Jones, U. Kruse, T. Roberts, B. Weinstein, and H. W. Wyld, Phys. Rev. D **9**, 1963 (1974).

[57] R. Aaron, R. S. Longacre, and J. E. Sacco, Ann. Phys. (N.Y.) **117**, 56 (1979).
[58] J. L. Basdevant and E. L. Berger, Phys. Rev. D **16**, 657 (1977).
[59] M. Albaladejo, D. Winney, I. V. Danilkin, C. Fernández-Ramírez, V. Mathieu, M. Mikhasenko, A. Pilloni, J. A. Silva-Castro, and A. P. Szczepaniak (JPAC Collaboration), Phys. Rev. D **101**, 054018 (2020).
[60] T. W. B. Kibble, Phys. Rev. **117**, 1159 (1960).
[61] P. D. B. Collins, *An Introduction to Regge Theory and High Energy Physics* (Cambridge University Press, Cambridge, England, 1977).
[62] V. N. Gribov, *The Theory of Complex Angular Momenta: Gribov Lectures on Theoretical Physics*, Cambridge Monographs on Mathematical Physics (Cambridge University Press, Cambridge, England, 2007).
[63] D. Stamen, D. Winney, A. Rodas, C. Fernández-Ramírez, V. Mathieu, G. Montaña, A. Pilloni, and A. P. Szczepaniak, Phys. Rev. D **110**, 114023 (2024).
[64] M. Hoferichter, B. Kubis, S. Leupold, F. Niecknig, and S. P. Schneider, Eur. Phys. J. C **74**, 3180 (2014).
[65] A. Jackura, C. Fernández-Ramírez, V. Mathieu, M. Mikhasenko, J. Nys, A. Pilloni, K. Saldaña, N. Sherrill, and A. P. Szczepaniak (JPAC Collaboration), Eur. Phys. J. C **79**, 56 (2019).
[66] S. M. Dawid, M. H. E. Islam, and R. A. Briceño, Phys. Rev. D **108**, 034016 (2023).
[67] R. Omnes, Nuovo Cimento **8**, 316 (1958).
[68] N. I. Muskhelishvili, *Singular Integral Equations* (Wolters-Noordhoff Publishing, 1958).
[69] J. Stern, H. Sazdjian, and N. H. Fuchs, Phys. Rev. D **47**, 3814 (1993).
[70] M. Albaladejo and B. Moussallam, Eur. Phys. J. C **77**, 508 (2017).
[71] F. E. Close and G. A. Schuler, Phys. Lett. B **464**, 279 (1999).
[72] L. Lesniak and A. P. Szczepaniak, Acta Phys. Pol. B **34**, 3389 (2003).
[73] A. Jackura *et al.* (JPAC, COMPASS Collaboration), Phys. Lett. B **779**, 464 (2018).
[74] D. Winney and A. P. Szczepaniak, arXiv:2512.21805.
[75] V. Mathieu, J. Nys, C. Fernández-Ramírez, A. Jackura, A. Pilloni, N. Sherrill, A. P. Szczepaniak, and G. Fox (JPAC Collaboration), Phys. Rev. D **97**, 094003 (2018).
[76] A. Aktas *et al.* (H1 Collaboration), Eur. Phys. J. C **46**, 585 (2006).
[77] M. Derrick *et al.* (ZEUS Collaboration), Z. Phys. C **69**, 39 (1995).
[78] M. Aghasyan *et al.* (COMPASS Collaboration), Phys. Rev. D **98**, 092003 (2018).
[79] G. Passarino and M. J. G. Veltman, Nucl. Phys. **B160**, 151 (1979).
[80] T. Hahn and M. Perez-Victoria, Comput. Phys. Commun. **118**, 153 (1999).
[81] A. W. Jackura and R. A. Briceño, Phys. Rev. D **109**, 096030 (2024).
[82] M. H. Akdag, C and *CP* violation in light-meson decays, Ph.D. thesis, U. Bonn (main), 2023.
[83] I. J. R. Aitchison, Phys. Rev. **137**, B1070 (1965).
[84] Bartl, Martin, Study of the $\pi^-\pi^+$ subsystem with $J^{PC} = 1^{--}$ in the diffractively produced $\pi^-\pi^+\pi^+$ final state at COMPASS, Master's thesis, Technische Universität München, 2023.
[85] M. Albaladejo *et al.* (JPAC Collaboration), Prog. Part. Nucl. Phys. **127**, 103981 (2022).
[86] A. Donnachie and P. V. Landshoff, Phys. Lett. B **296**, 227 (1992).
[87] A. N. Hiller Blin, C. Fernández-Ramírez, A. Jackura, V. Mathieu, V. I. Mokeev, A. Pilloni, and A. P. Szczepaniak, Phys. Rev. D **94**, 034002 (2016).
[88] A. Jackura, M. Mikhasenko, and A. Szczepaniak, EPJ Web Conf. **130**, 05008 (2016).
[89] M. Mikhasenko, A. Jackura, B. Ketzer, and A. Szczepaniak (COMPASS Collaboration), EPJ Web Conf. **137**, 05017 (2017).
[90] E. Klempt and A. Zaitsev, Phys. Rep. **454**, 1 (2007).
[91] J. J. Dudek, Phys. Rev. D **84**, 074023 (2011).
[92] Y. Feng, F. Gil, M. Döring, R. Molina, M. Mai, V. Shastry, and A. Szczepaniak, Phys. Rev. D **110**, 094002 (2024).
[93] D. Sadasivan, A. Alexandru, H. Akdag, F. Amorim, R. Brett, C. Culver, M. Döring, F. X. Lee, and M. Mai, Phys. Rev. D **105**, 054020 (2022).
[94] R. Molina, M. Doering, W. H. Liang, and E. Oset, Eur. Phys. J. C **81**, 782 (2021).
[95] M. Nozar *et al.* (CLAS Collaboration), Phys. Rev. Lett. **102**, 102002 (2009).
[96] A. Tsaris, A study of 3π production in $\gamma p \to n\pi^+\pi^+\pi^-$ and $\gamma p \to \Delta^{++}\pi^+\pi^-\pi^-$ with CLAS at Jefferson Lab, Ph.D. thesis, Florida State U., 2016.
[97] C. Bookwalter, A search for exotic mesons in $\gamma p \to \pi^+\pi^+\pi^- n$ with CLAS at Jefferson Lab, Ph.D. thesis, Florida State U., 2012.
[98] A. P. Szczepaniak and M. Swat, Phys. Lett. B **516**, 72 (2001).
[99] A. V. Afanasev and A. P. Szczepaniak, Phys. Rev. D **61**, 114008 (2000).
[100] F. E. Close and J. J. Dudek, Phys. Rev. D **70**, 094015 (2004).
[101] M. Albrecht (GlueX Collaboration), Nuovo Cimento C **47**, 181 (2024).
[102] F. Niecknig and B. Kubis, Phys. Lett. B **780**, 471 (2018).
[103] E. Kou, T. Moskalets, and B. Moussallam, J. High Energy Phys. 12 (2023) 177.
[104] F. Niecknig and B. Kubis, J. High Energy Phys. 10 (2015) 142.
[105] T. Isken, B. Kubis, S. P. Schneider, and P. Stoffer, Eur. Phys. J. C **77**, 489 (2017).
[106] H. Akdag, T. Isken, and B. Kubis, J. High Energy Phys. 02 (2021) 137; 12 (2022) 156(E).
[107] X.-Y. Hu, J. He, P. Niu, Q. Wang, and Y. Yan, Phys. Rev. D **113**, 054003 (2026).
[108] R. Abdul Khalek *et al.*, Nucl. Phys. **A1026**, 122447 (2022).
[109] A. Accardi *et al.*, Eur. Phys. J. A **60**, 173 (2024).
[110] D. Winney, iterateKT (v1.1) (2026), 10.5281/zenodo.23426016.
[111] D. Winney, bootstrapPi1 (v1.0) (2026), 10.5281/zenodo.23491460.
[112] C. Kacser, Phys. Rev. **132**, 2712 (1963).

[113] T. L. Trueman and G. C. Wick, Ann. Phys. (N.Y.) **26**, 322 (1964).
[114] E. Byckling and K. Kajantie, *Particle Kinematics* (University of Jyvaskyla, Jyvaskyla, Finland, 1971).
[115] M. Abramowitz and I. A. Stegun, *Handbook of Mathematical Functions with Formulas, Graphs, and Mathematical Tables*, ninth dover printing, tenth gpo printing ed. (Dover, New York, 1964).
[116] G. Montana *et al.* (Joint Physics Analysis Center Collaboration), Phys. Rev. D **110**, 114012 (2024).
[117] I. J. R. Aitchison and C. Kacser, Nuovo Cimento A **40**, 576 (1965).
[118] L. Bibrzycki, C. Fernandez-Ramirez, V. Mathieu, M. Mikhasenko, M. Albaladejo, A. N. H. Blin, A. Pilloni, and A. P. Szczepaniak (JPAC Collaboration), Eur. Phys. J. C **81**, 647 (2021); **81**, 915(E) (2021).
[119] H. Pekeler (COMPASS Collaboration), Proc. Sci. HADRON2025 (**2026**) 152.
[120] H. Pekeler, Production of $\eta\pi^-$ and $\eta'\pi^-$ final states in high energy $\pi^- p$ scattering at COMPASS, Ph.D. thesis, Bonn Universität, 2025.
[121] G. D. Alexeev *et al.* (COMPASS, JPAC Collaboration), First Observation of an Exotic Reggeon, arXiv:2607.17850.
[122] R. Garcia-Martin, R. Kaminski, J. R. Pelaez, J. Ruiz de Elvira, and F. J. Yndurain, Phys. Rev. D **83**, 074004 (2011).
[123] V. Gribov, *Strong Interactions of Hadrons at High Energies: Gribov Lectures on Theoretical Physics* (Oxford University Press, New York, 2009).
[124] M. Froissart, Phys. Rev. **123**, 1053 (1961).
[125] G. Montaña *et al.*, Phys. Lett. B **872**, 140101 (2026).
[126] R. Barsotti, Photoproduction of $\eta\pi^0$ by double-Regge exchange, Ph.D. thesis, Indiana University, Bloomington IN, USA, 2025.
[127] T. Shimada, A. D. Martin, and A. C. Irving, Nucl. Phys. **B142**, 344 (1978).